


# Cysteine Enrichment Mediates Co-Option of Uricase in Reptilian Skin and Transition to Uricotelism

Giulia Mori <sup>\*,†,1</sup>, Anastasia Liuzzi,<sup>†,1</sup> Luca Ronda,<sup>2</sup> Michele Di Palma,<sup>3</sup> Magda S. Chegkazi,<sup>4</sup> Soi Bui,<sup>4</sup> Mitla Garcia-Maya,<sup>4</sup> Jasmine Ragazzini,<sup>1</sup> Marco Malatesta,<sup>1</sup> Emanuele Della Monica,<sup>1</sup> Claudio Rivetti,<sup>1</sup> Parker B. Antin,<sup>5</sup> Stefano Bettati,<sup>2</sup> Roberto A. Steiner,<sup>\*,3,4</sup> and Riccardo Percudani<sup>\*,1</sup>

<sup>1</sup>Department of Chemistry, Life Sciences and Environmental Sustainability, University of Parma, Parma, Italy

<sup>2</sup>Department of Medicine and Surgery, University of Parma, Parma, Italy

<sup>3</sup>Department of Biomedical Sciences, University of Padova, Padova, Italy

<sup>4</sup>Randall Centre for Cell and Molecular Biophysics, King's College London, London, UK

<sup>5</sup>Department of Cellular and Molecular Medicine, University of Arizona, Tucson, USA

<sup>†</sup>These authors contributed equally to this work.

\*Corresponding authors: E-mails: giulia.mori@unipr.it; roberto.steiner@kcl.ac.uk; riccardo.percudani@unipr.it.

Associate editor: Dr. Fabia Ursula Battistuzzi

## Abstract

Uric acid is the main means of nitrogen excretion in uricotelic vertebrates (birds and reptiles) and the end product of purine catabolism in humans and a few other mammals. While uricase is inactivated in mammals unable to degrade urate, the presence of orthologous genes without inactivating mutations in avian and reptilian genomes is unexplained. Here we show that the *Gallus gallus* gene we name cysteine-rich urate oxidase (CRUOX) encodes a functional protein representing a unique case of cysteine enrichment in the evolution of vertebrate orthologous genes. CRUOX retains the ability to catalyze urate oxidation to hydrogen peroxide and 5-hydroxyisourate (HIU), albeit with a 100-fold reduced efficiency. However, differently from all uricases hitherto characterized, it can also facilitate urate regeneration from HIU, a catalytic property that we propose depends on its enrichment in cysteine residues. X-ray structural analysis highlights differences in the active site compared to known orthologs and suggests a mechanism for cysteine-mediated self-aggregation under H<sub>2</sub>O<sub>2</sub>-oxidative conditions. Cysteine enrichment was concurrent with the transition to uricotelism and a shift in gene expression from the liver to the skin where CRUOX is co-expressed with  $\beta$ -keratins. Therefore, the loss of urate degradation in amniotes has followed opposite evolutionary trajectories: while uricase has been eliminated by pseudogenization in some mammals, it has been repurposed as a redox-sensitive enzyme in the reptilian skin.

**Key words:** uricase, metabolic adaptation, nitrogen elimination, orthologous gene divergence, sauropsids.

## Introduction

Uricase or urate oxidase (Uox) is an evolutionarily conserved enzyme of ancient origin that is found in all three domains of life. In vertebrates, it acts in the liver peroxisomes (Hayashi et al. 2000) by converting the purine catabolic product uric acid to 5-hydroxyisourate (Kahn and Tipton 1998; Bui et al. 2014). Depending on the species, purine degradation proceeds further to give allantoin or urea (Noguchi et al. 1979; Dembech et al. 2023) as nitrogen waste products that are excreted from the body through urine. In various species, however, the end product is the poorly soluble uric acid.

Truncation of purine degradation to uric acid coupled with de novo purine synthesis allows uricotelic animals to eliminate nitrogenous waste through minimal water consumption (Campbell et al. 1987; Wright 1995; Salway 2018). Among vertebrates, uricotelism is a monophyletic

trait of sauropsids (birds and reptiles), which excrete both amino acid and purine nitrogen in the form of uric acid. Although uric acid is the end product of purine degradation also in some mammals, including humans, these organisms excrete mainly urea (ureotelism). Fish and amphibians, on the other hand, excrete mainly ammonia (ammonotelism), as do invertebrate deuterostomes (fig. 1).

The different strategies of nitrogen elimination in vertebrates exemplify the metabolic adaptations associated with different living environments. Nitrogen disposal in the form of ammonia can be accomplished by aquatic vertebrates as large amounts of water are required to maintain ammonia concentrations below toxic levels. Vertebrates that tolerate a dry environment convert ammonia into compounds (urea or uric acid) that can be more concentrated than ammonia in body fluids. Excretion of urea requires about ten times less water

© The Author(s) 2023. Published by Oxford University Press on behalf of Society for Molecular Biology and Evolution.

This is an Open Access article distributed under the terms of the Creative Commons Attribution License (<https://creativecommons.org/licenses/by/4.0/>), which permits unrestricted reuse, distribution, and reproduction in any medium, provided the original work is properly cited.

Open Access

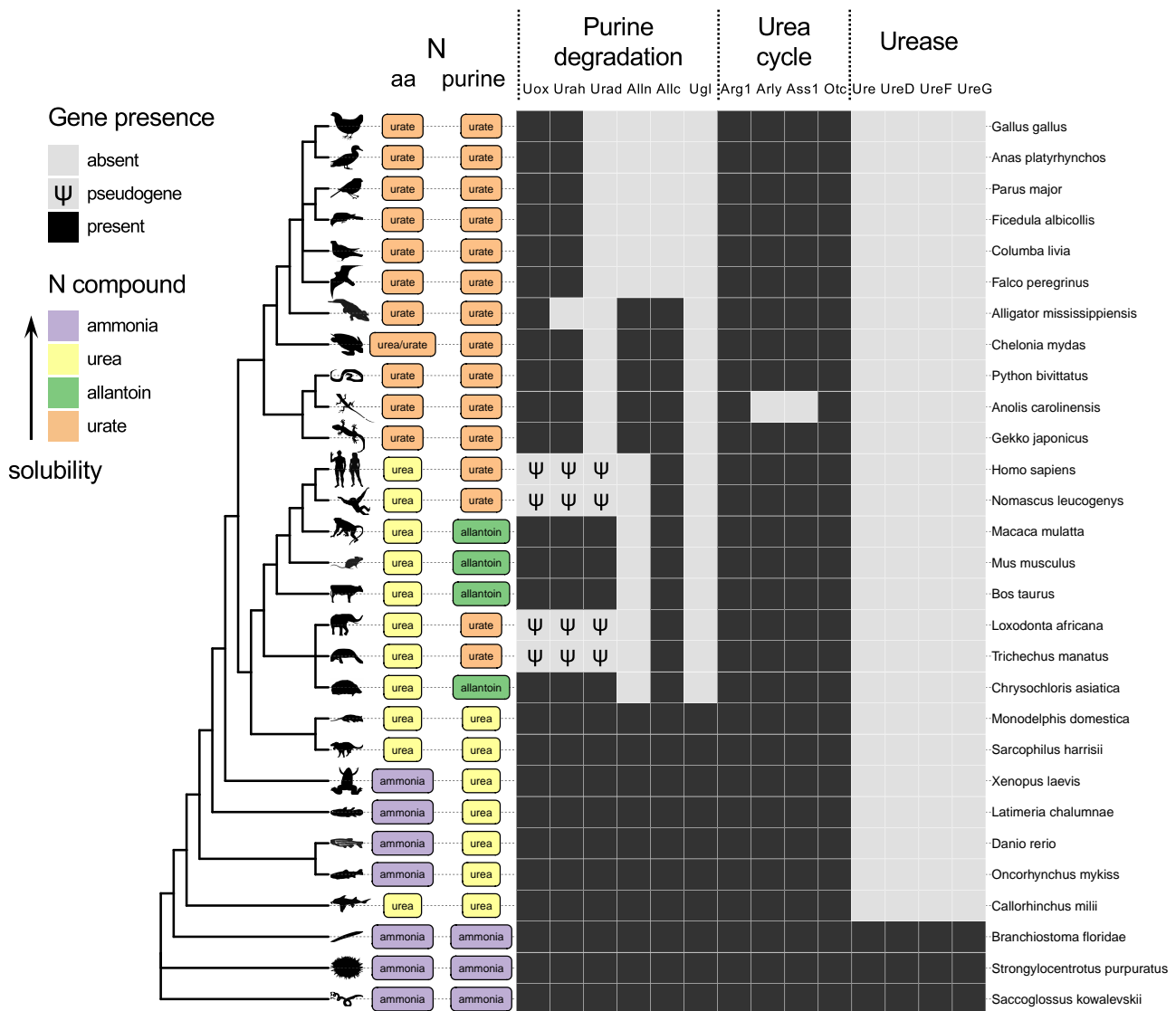


**Fig. 1.** Nitrogen elimination in aquatic and terrestrial deuterostomes. Scheme of the main nitrogenous end product of amino acid and purine metabolism in vertebrate and invertebrate deuterostomes across the NCBI phylogeny of selected species with emphasis on vertebrates. The presence of genes relevant for the metabolism of urea and uric acid is indicated by black boxes. Pseudogenes are indicated by a Ψ symbol. The main nitrogenous waste product of amino acid and purine metabolism is indicated based on literature evidence and/or genetic content ([supplementary file S1, Supplementary Material](#) online). PhyloPic silhouettes (<http://phylopic.org>) are added to selected branches to aid species identification.

than ammonia, whereas the highly insoluble uric acid requires about 50 times less water ([Wright 1995](#)). Indeed, ureotelism and uricotelism have been two routes of adaptation to terrestrial life; in particular, uricotelism contributed to the radiation of reptiles during the Triassic Period providing them with the ability to tolerate the extremely dry Triassic climate ([Campbell et al. 1987](#)). It has been noted that this advantage comes at the expense of energy consumption since about four phosphoanhydride ATP bonds are required for each nitrogen atom to convert ammonia to uric acid, compared with two required for its conversion to urea ([Salway 2018](#)). Even though vertebrates are unable to recycle nitrogen contained in urea or uric acid, this capacity can be provided by intestinal microbes that degrade urea and uric acid to generate ammonia as a nitrogen

source. This nitrogen conservation mechanism may be relevant in conditions of limited nitrogen intake ([Singer 2003](#)).

In addition to water conservation, the truncation of purine degradation to uric acid, which ultimately led to the development of uricotelism in sauropsids, is thought to have provided at least one more selective advantage, due to the antioxidant properties of uric acid ([Simic and Jovanovic 1989](#)). The atmosphere at the time of reptiles radiation was more strongly oxidizing than is today and sauropsids, having a blood content of uric acid more than five-fold higher than that of ureotelic vertebrates ([Dessauer 1970](#)), may have had a selective advantage under those conditions. It has been suggested that the antioxidant properties of uric acid are the reason why the loss of uricase occurred in apes, especially after the loss in

Haplorhini primates of the ability to synthesize the antioxidant ascorbic acid (Ames et al. 1981; Nishikimi et al. 1994). An evolutionary cost of high levels of uric acid is the formation of crystalline precipitate in the kidney and joints and the development of a painful arthritis known as gout. Similarly to humans, birds and reptiles suffer gout (Peterson et al. 1971; Rothschild et al. 2013), a disease which also affected dinosaurs according to the fossil record (Rothschild et al. 1997).

Truncation of purine degradation in apes was caused by *Uox* pseudogenization through nonsense mutations (Wu et al. 1989; Oda et al. 2002), possibly preceded by a missense mutation increasing the enzyme  $K_M$  for the urate substrate (Kratzer et al. 2014; Marchetti et al. 2016; Li et al. 2022). These events were accompanied by pseudogenization of the other two genes involved in the conversion of uric acid to allantoin, HIU hydrolase (*Urah*), and OHCU decarboxylase (*Urad*), through inactivating mutations of the coding sequence and transcriptional promoter (Ramazzina et al. 2006; Keebaugh and Thomas 2010). A similar pattern of pseudogenization (fig. 1) has been recently identified in elephants and manatee (Tethytheria), suggesting convergent loss of urate degradation in these mammals (Sharma and Hiller 2020). By contrast, although liver uricase is absent in uricotelic organisms, no inactivating mutations are found in the *Uox* gene, which appears to be universally conserved in sauropsids (fig. 1). This conservation suggests that the gene is still subjected to selection pressure, as also supported by a low  $K_a/K_s$  ratio (Keebaugh and Thomas 2010). Overall, these lines of evidence point to the possibility that reptilian uricase has been repurposed for a different function concurrently with transition to uricotelism, more than 300 Ma. Gene co-option, that is the establishment of a new use for an existing gene, is known to be an important mechanism in vertebrate evolution (True and Carroll 2002; McLennan 2008), but whether it has a role in the transition to uricotelism and maintenance of uricase in sauropsids is unknown.

To understand the biological significance of uricase maintenance in sauropsids, we studied the gene and protein from the model organism *Gallus gallus*. We found evidence that uricase has been repurposed as a redox-sensitive enzyme in the skin of uricotelic vertebrates. By a large-scale analysis, we also found that co-option of uricase in the reptilian ancestor was mediated by an increase in the cysteine content that is unmatched in the evolution of vertebrate orthologous genes.

## Results

### Distinct Sequence Alterations in Reptilian *Uox* Genes

Alignment of *Uox* sequences (fig. 2A) revealed conservation of the active site residues in reptilian proteins with a single exception: a tyrosine substitutes a valine in position 230 of *Gallus gallus* *Uox*. In contrast, the N and C termini are visibly different between reptilian and nonreptilian *Uox*. Differences in the N-terminal regions

are due to modification in the exon-intron structure of vertebrate *Uox* genes (fig. 2B). In spite of the conserved synteny between *Uox* and *Dnase2b* in vertebrates (fig. 2B), it was previously noted that the first *Uox*-coding exon mapped to a distinct location in some birds (Keebaugh and Thomas 2010). Although the amino acid sequence encoded by the first exon is not conserved between avian and nonavian reptiles (fig. 2A), the exon-intron structure of the *Uox* locus in reptiles is the same, wherein the first exon lies upstream of the neighbor *Dnase2b* gene (first two species in fig. 2B). Even in cases (e.g., *Anolis carolinensis*) in which the transcription start site of *Uox* is reported downstream of *Dnase2b*, the existence of the upstream exon could be demonstrated by the alignment of the Expressed Sequence Tag sequences (supplementary fig. S1, Supplementary Material online). Therefore, the first exon of vertebrate *Uox*, which lies downstream of the bidirectional promoter shared with the divergently oriented *Dnase2b* gene (last two species in fig. 2B), was probably lost in the reptile ancestor and a new one was acquired upstream of the 3' end of *Dnase2b*, together with a new promoter. At the C terminus, the peroxisome targeting signal (PTS1) present in eukaryotic *Uox* is absent owing to the addition of an extra peptide of ~20 amino acids (fig. 2A). This suggests that *Uox* is not a peroxisomal protein in reptiles.

A striking difference is found in the content of cysteine residues, that in reptilian *Uox* is about five-fold higher than that of nonreptilian *Uox* (~5% vs. ~1%), including metazoan, fungal, plant, and bacterial sequences (fig. 2C). Cysteines appear evenly distributed along the reptilian *Uox* sequence and not always conserved across species (fig. 2A).

### Unique Increase in Cysteine Content in Reptilian *Uox*

Intrigued by the enrichment of cysteines in reptilian *Uox* sequences, we analyzed the variation in amino acid composition of orthologous proteins in vertebrates. We used a large set of orthologous groups (orthogroups) retrieved from the database OrthoDB, which was filtered to include only single-copy genes and orthogroups present in at least 90% of genomes. The selected dataset contained 3,393 orthogroups and 745,945 sequences distributed over three vertebrate clades: Sauropsida, Mammalia, and Actinopterygii. For the three taxonomic groups, the mean content of each amino acid in each orthogroup was analyzed through pairwise comparisons (Sauropsida-Mammalia; Sauropsida-Actinopterygii; Mammalia-Actinopterygii). Orthogroups with significant variation in amino acid content were identified by using a *P*-value cutoff of  $1e-16$  and a fold-change cutoff of  $\pm 1$ .

Only a few orthogroups were found to be significantly differentiated in cysteine content between the three group pairs: three between Sauropsida and Mammalia (fig. 3A), nine between Sauropsida and Actinopterygii (fig. 3B), and eight between Mammalia and Actinopterygii (supplementary fig. S2A and table S1, Supplementary

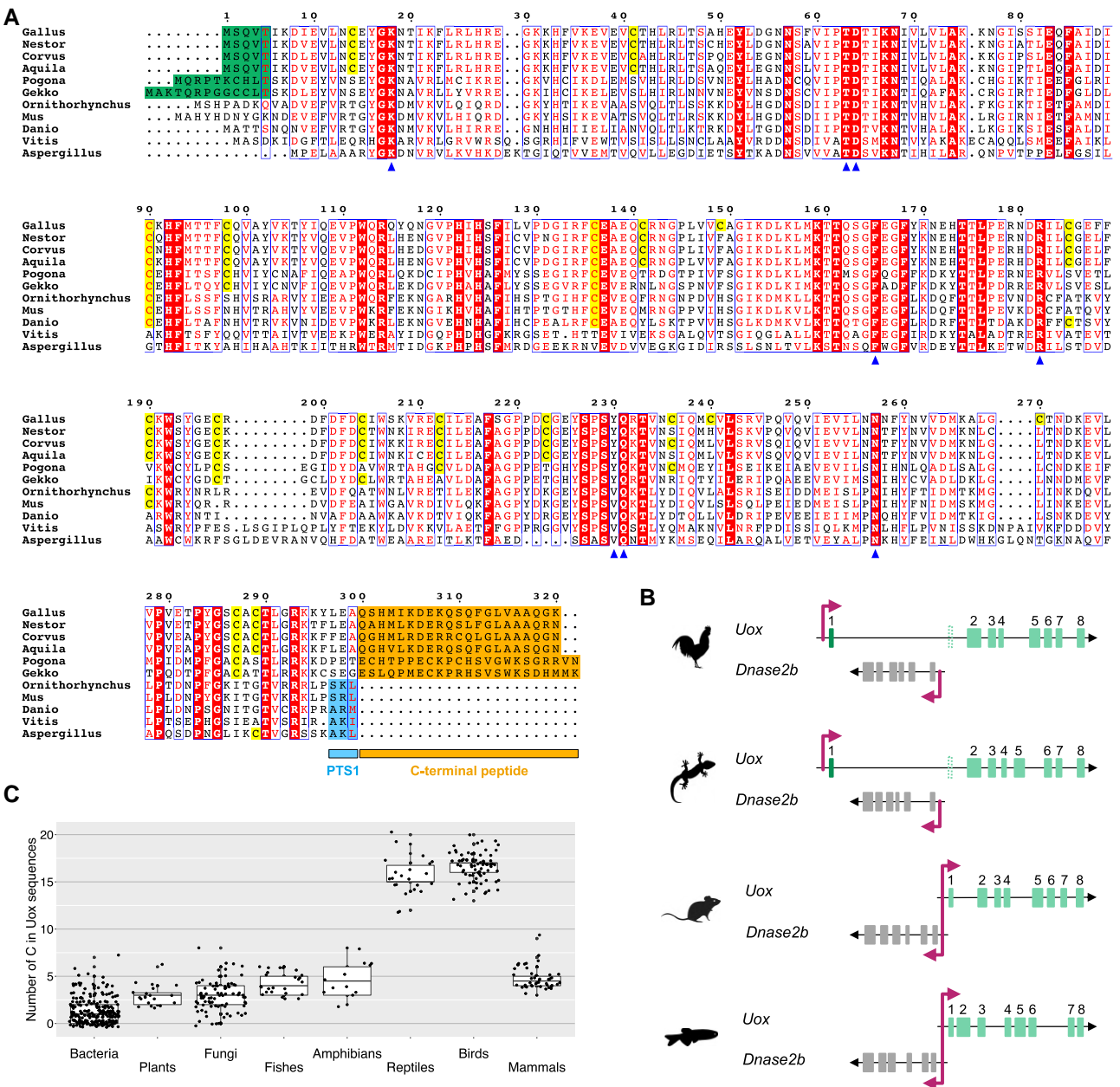


**Fig. 2.** Distinct sequence alterations in reptilian *Uox* genes. (A) Multiple alignment of *Uox* sequences from different eukaryotic species, showing conservation of active site residues (blue arrowheads) together with diversification in cysteine content and in the C-terminal region. Cysteines of *Gallus gallus* *Uox* and cysteines that are conserved in the other sequences are highlighted in yellow. The N-terminal sequence encoded by the first exon in reptilian *Uox* is highlighted in dark green; the C-terminal peptide in reptilian *Uox* is highlighted in orange; the tripeptide corresponding to PTS1 in non-reptilian *Uox* is highlighted in light blue. (B) Gene structure of *Uox* and *Dnase2b* from *Gallus gallus* (*Uox*: LOC101747367), *Gekko japonicus* (*Uox*: LOC107117302), *Mus musculus*, and *Danio rerio*, showing absence of a bidirectional promoter in sauropsids, and presence in the other vertebrates. (C) Boxplots illustrating cysteine abundance in *Uox* sequences of different taxonomic groups. Median (thick lines), first and third quartile (thin lines) of the number of cysteines in individual *Uox* sequences (black circles) grouped according to taxonomy. Here, the term “reptiles” refers to nonavian reptile species.

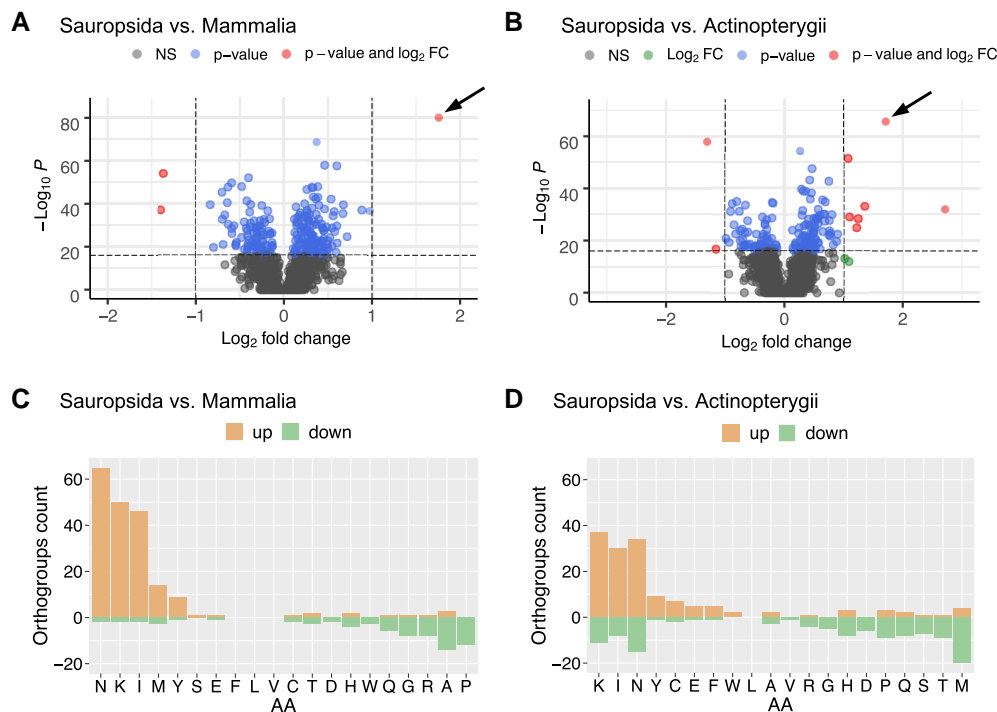
Material online). Interestingly, the *Uox* orthogroup stands out as an exceptional case of cysteine enrichment in the evolution of orthologous genes in amniotes (fig. 3A and 3B, arrows).

In our analysis, we observed that glycine, leucine, valine, phenylalanine, tryptophan, glutamine, serine, threonine, tyrosine, aspartate, glutamate, arginine, and histidine followed the same trend of cysteine, as they have emerged

as significantly varying in a few (<10) or no orthogroups across the three vertebrate clades (figs. 3C and D and supplementary fig. S2B, Supplementary Material online). In contrast, isoleucine, asparagine, and lysine (INK) appeared to vary significantly in a greater number of orthogroups (>50) in each of the three pairwise comparisons. In particular, the three amino acids are increased in reptiles (figs. 3C and D and supplementary fig. S3, Supplementary Material



**FIG. 3.** Amino acid content variation in vertebrate orthologous proteins. (A and B) Volcano plot depicting the cysteine content variation of orthologous proteins between groups of vertebrates: (A) sauropsids versus mammals, and (B) sauropsids versus fishes. Horizontal dashed line indicates  $P$ -value of  $10^{-16}$ ; vertical dashed lines indicate  $\log_2$  fold change of  $-1$  and  $1$ . The Uox orthogroup, in which the cysteine content is significantly increased, is indicated by an arrow. Orthogroup names and numeric values are reported in [supplementary table S1](#), [Supplementary Material](#) online. (C and D) Bar plot illustrating the number of orthogroups in which the content of the corresponding amino acid is significantly increased (light orange) or decreased (green) according to  $P$ -value  $< 10^{-16}$  and  $\log_2$  fold change  $> \pm 1$  in (C) sauropsids versus mammals, and (D) sauropsids versus fishes.



online); asparagine is also decreased in fishes with respect to mammals ([supplementary fig. S2B](#), [Supplementary Material](#) online). Of the remaining amino acids, methionine is increased in some piscine orthogroups ([fig. 3D](#) and [supplementary fig. S2B](#), [Supplementary Material](#) online); alanine and proline are increased in some mammalian orthogroups ([fig. 3C](#) and [supplementary fig. S2B](#), [Supplementary Material](#) online).

### GgUox Catalyzes the Oxidation of Urate and the Reduction of 5-HIU

To investigate the activity of reptilian uricase, we overexpressed the coding sequence of *Gallus gallus* Uox (GgUox) in *E. coli* and purified the corresponding protein to apparent homogeneity using either xanthine-agarose ([fig. 4A](#)) or nickel affinity columns ([supplementary fig. S4A](#), [Supplementary Material](#) online). The binding to a stationary phase with a specific affinity for uricase ([Nishimura et al. 1982](#)) provides evidence that GgUox has a preserved purine-binding ability. The purified protein was eluted as a single peak compatible with a tetramer in size-exclusion chromatography (SEC) ([supplementary fig. S4B](#), [Supplementary Material](#) online). The enzyme catalyzed the oxidation of uric acid (UA) to 5-hydroxyisourate (HIU) and hydrogen peroxide and exhibited Michaelis-Menten kinetics at increasing substrate concentrations ([fig. 4B](#)). However, despite a  $K_M$  ( $12.5 \mu\text{M}$ ) comparable to that of *Danio rerio* Uox (*DrUox*) ( $11 \mu\text{M}$ ) ([Marchetti et al. 2016](#)), the turnover number ( $k_{\text{cat}}$ ) is  $>100$ -fold lower ( $0.03 \text{ s}^{-1}$  for GgUox vs.  $3.95 \text{ s}^{-1}$  for *DrUox*). Consistently,

the kinetics of hydrogen peroxide formation coupled to the oxidation of urate in single turnover conditions is slower in the presence of GgUox than in the presence of *DrUox* ([figs. 4C](#) and [supplementary fig. S4C](#), [Supplementary Material](#) online).

Accumulation of the unstable oxidation product, HIU, can be detected as a shift of the urate peak from 292 to 301 nm during the *DrUox* reaction ([supplementary fig. S5A](#), [Supplementary Material](#) online). In the case of GgUox, HIU accumulation was less noticeable ([fig. 4D](#)), but when an enzyme with HIU hydrolase activity (allantoin synthase; Alls) was added, the reaction reached completion at an initial rate about three-fold faster ([fig. 4E](#)). This behavior suggests a possible reconversion of HIU to urate that has been described for uricase catalysis in the presence of a reducing agent, such as dithiothreitol (DTT) or cysteine ([Sarma and Tipton 2000](#)). When the GgUox reaction was conducted in the presence of  $\beta$ -mercaptoethanol ( $\beta\text{ME}$ ), the oxidation of urate to HIU was extremely slow ([fig. 4F](#)), and, again, the addition of Alls resulted in the completion of the reaction at an initial rate comparable to that in the absence of the reducing agent ([fig. 4G](#)). In contrast, the *DrUox* activity under the same reducing conditions was almost unaffected ([supplementary fig. S5B](#), [Supplementary Material](#) online). This suggests that  $\beta\text{ME}$ , while unable to reduce HIU, can reduce GgUox cysteines that are significantly more abundant than in *DrUox*. To confirm the reconversion reaction, we isolated enzymatically generated HIU and monitored its reduction back to urate in the presence of either GgUox and  $\beta\text{ME}$  ([fig. 4H](#)) or *DrUox* and  $\beta\text{ME}$

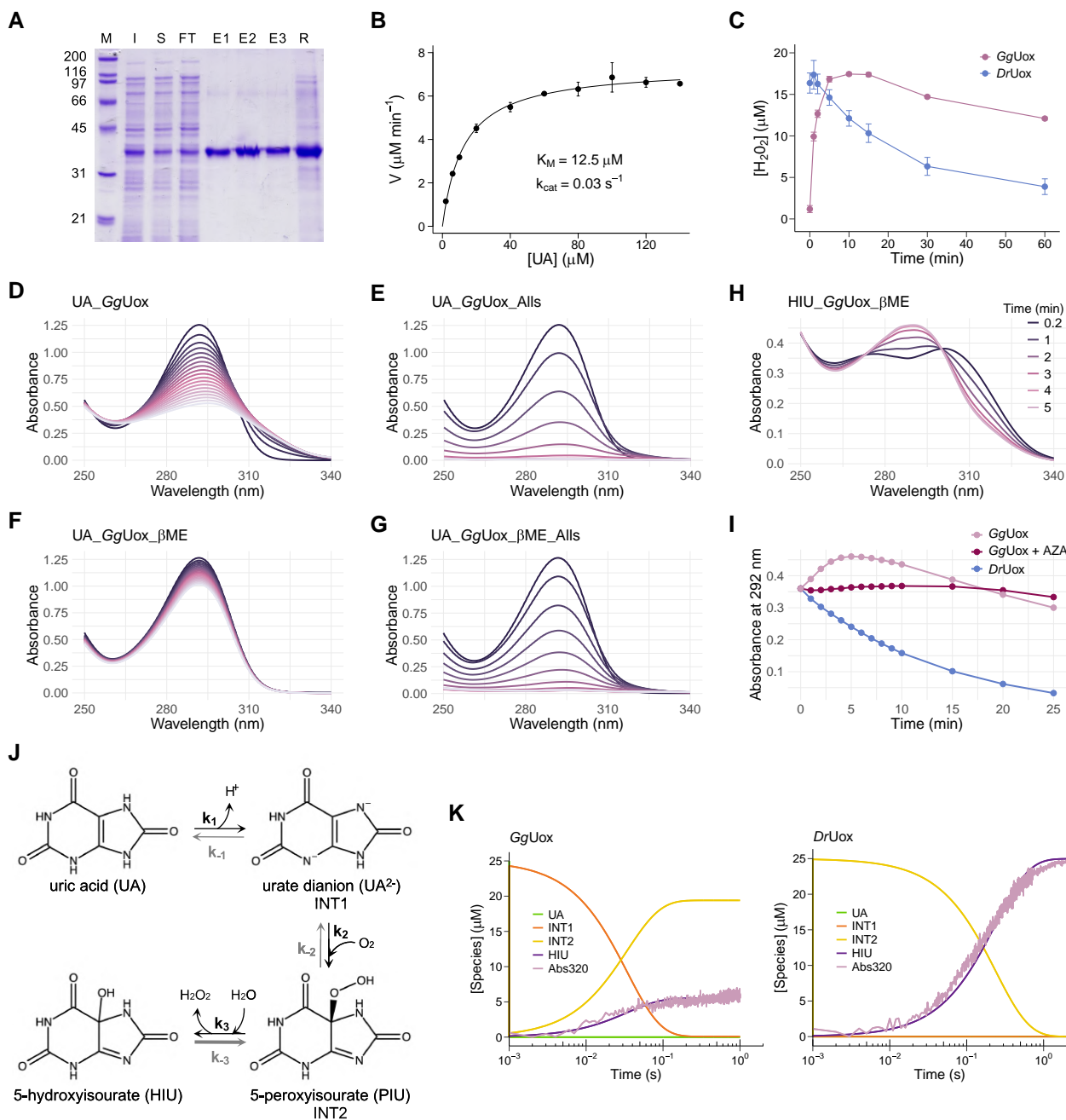


**FIG. 4.** Uricase activity of *Gallus gallus* Uox. (A) SDS-PAGE of the purification of GgUox by xanthine-agarose affinity chromatography. M: marker; I: postinduction total cell fraction; S: soluble cell fraction; FT: flow-through; E1–E3: elution fractions; R: resin. (B) Michaelis–Menten dependencies of GgUox uricase activity on uric acid (UA) concentration. Kinetic measurements were carried out in 100 mM potassium phosphate (pH 7.6), at 25°C, using 4.1  $\mu\text{M}$  GgUox and 1  $\mu\text{M}$  HIU hydrolase (HIUase). (C) Kinetics of hydrogen peroxide turnover in the urate oxidation reaction catalyzed by GgUox or DrUox. Reactions were carried out under single turnover conditions with 100 mM potassium phosphate (pH 7.6), 30  $\mu\text{M}$  enzyme, 25  $\mu\text{M}$  UA. The amount of hydrogen peroxide was quantified by FOX assay. (D–G) Time-resolved UV–Vis spectra of urate oxidation by GgUox. (D) Reaction mixture contained 100 mM potassium phosphate (pH 7.6), 30  $\mu\text{M}$  GgUox, and 100  $\mu\text{M}$  UA. (E–G) Reaction mixtures were the same as in (D) with the addition of (E) 1.25  $\mu\text{M}$  allantoin synthase (Alls), (F) 300  $\mu\text{M}$   $\beta$ -mercaptoethanol ( $\beta\text{ME}$ ), (G) 1.25  $\mu\text{M}$  Alls and 300  $\mu\text{M}$   $\beta\text{ME}$ . Spectra were acquired every 1 min at 25°C. (H) Time-resolved UV–Vis spectra of 5-hydroxyisourate (HIU) degradation by GgUox. Reaction contained 100 mM potassium phosphate (pH 7.6), 60  $\mu\text{M}$  HIU, 30  $\mu\text{M}$  GgUox, and 300  $\mu\text{M}$   $\beta\text{ME}$ . Spectra were acquired every 1 min at 25°C. (I) Time-dependent change of absorbance at 292 nm during HIU degradation by GgUox (pink), GgUox with 8-azaxanthine (AZA; bordeaux), and DrUox (light blue). Reaction mixtures were the same as in (H); AZA was 50  $\mu\text{M}$ . (J) Three-steps reversible model for UA to HIU conversion. Intermediate species were already attributed to urate dianion ( $\text{UA}^{2-}$ ) and 5-peroxyisourate (PIU) (Kahn and Tipton 1998). (K) Experimental stopped-flow kinetics (“Abs320”: pink) of GgUox (left) or DrUox (right) reaction and fitting to three-steps reversible model for UA to HIU conversion. Reactions were carried out under single turnover conditions at 25°C with 100 mM potassium phosphate (pH 7.6), 35  $\mu\text{M}$  enzyme, and 25  $\mu\text{M}$  UA.

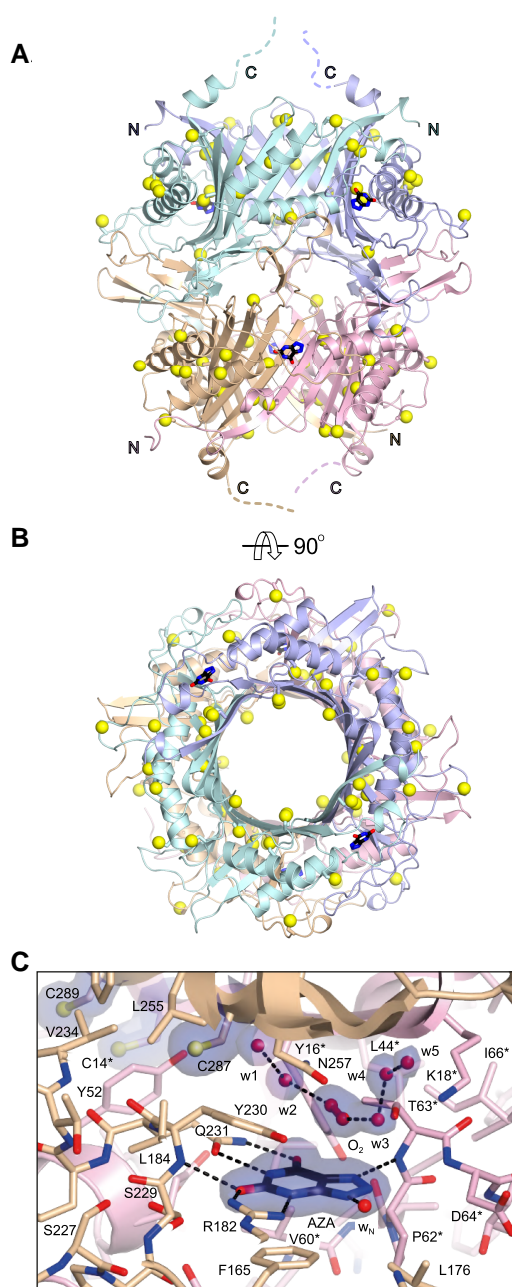


**FIG. 5.** X-ray structure of Cys-rich GgUox. (A–B) Side (A) and top (B) cartoon representations of the 146.5 kDa GgUox tetramer with the four protomers highlighted by different colors. The N and C termini of the different chains are indicated by the letters N and C, respectively. The flexible C-terminal regions corresponding to the last 18–20 amino acids are indicated in (A) by broken lines. Bound AZA ligands at the dimers' interface are shown as sticks. Cysteine residues are also shown as sticks with their SG atoms highlighted by yellow spheres. (C) Stick representation of AZA (black) bound in the active site at the interface between two different GgUox protomers, shown in wheat and pink for chain A and chain B, respectively.  $O_2$  and water molecules (labeled w1–5) closest to AZA are represented by spheres.  $2mF_o - DF_c$  electron density map for AZA, cysteines, and the solvent above the inhibitor is shown in blue at the 1.0  $\sigma$  level. Residues labeled with an asterisk indicate that they belong to a different Uox protomer. Cysteine residues in proximity are also shown with their SG atoms highlighted by spheres. Nitrogen, oxygen, and sulfur atoms are in blue, red, and yellow, respectively. Hydrogen bonds are shown by broken black lines.

(supplementary fig. S6A, Supplementary Material online). Only with GgUox we observed the shift of the HIU peak to 292 nm, indicating the formation of urate; with DrUox, HIU degraded spontaneously in a time-dependent manner similarly to without enzymes (supplementary fig. S6B, Supplementary Material online). The recycling of urate during GgUox (and not DrUox) reaction may be explained by the increased cysteine content of GgUox.

To assess the involvement of GgUox active site residues in the reduction of HIU, we repeated the experiment in the presence of 8-azaxanthine (AZA; supplementary fig. S6C, Supplementary Material online), a competitive inhibitor of uricase activity (Heitaroh et al. 1973) acting on GgUox as well (supplementary fig. S7, Supplementary Material online). In this case, the reconversion of HIU to urate is slower because, despite the shift of the HIU peak to 292 nm (supplementary fig. S6C, Supplementary Material online), we did not observe a similar increase of absorbance at 292 nm as in the reaction without the inhibitor (fig. 4I). However, the disappearance of HIU, as monitored by absorbance decrease at 315 nm, is faster than that in the presence of DrUox (supplementary fig. S6D, Supplementary Material online). These results suggest that the enzymatic regeneration of urate from HIU depends at least in part on the oxidoreductase activity at the GgUox active site.

GgUox activity was also investigated following urate degradation under single turnover conditions (25  $\mu$ M urate in the presence of excess GgUox—35  $\mu$ M) upon rapid mixing with a stopped-flow apparatus; the same experiment was carried out with DrUox for comparison. In agreement with the results described above, the observed kinetics indicated clear differences between GgUox and DrUox reactions. We observed that only ~20% HIU is formed in the presence of GgUox compared to DrUox (supplementary fig. S8A, Supplementary Material online). Singular value decomposition (SVD) on data matrices of kinetic traces for both enzymes showed a first spectral component, accounting for the large majority of the signal, with a negative peak centered at 294 nm and a positive peak at 314 nm (supplementary fig. S8B, Supplementary Material online, blue and light blue lines). This analysis allowed us to define a wavelength (320 nm) where only this component contributes to the kinetics (supplementary fig. S8B, Supplementary Material online, orange and yellow lines). Single wavelength kinetics at 320 nm were then evaluated in terms of a three-step sequential model previously proposed for uricase-catalyzed reaction (Kahn and Tipton 1998), considering reversible (fig. 4J) or irreversible (supplementary fig. S9A, Supplementary Material online) processes. In this model, the first intermediate is a urate dianion ( $UA^{2-}$ ) and the second intermediate is 5-peroxyisourate (PIU). Noteworthy, based on the previously reported spectra of Uox reaction intermediates (Kahn and Tipton 1998), the first SVD component corresponds to the difference spectrum between PIU and HIU (supplementary fig. S8C, Supplementary Material online). We confidently attribute the time-evolution of this SVD component to this direct conversion. For DrUox,



irreversible steps were successfully applied to fit the experimental data (fig. 4K, right panel), indicating that the forward reaction rates are much faster than the reverse reaction rates (supplementary fig. S9B, Supplementary Material online). We observed that while urate oxidation promptly proceeds to PIU, as the concentration of this second intermediate is maxima at the very beginning of the reaction (fig. 4K, yellow line in right panel), the final conversion to HIU is the rate-limiting step, with a rate constant ( $4.11 \pm 0.02 \text{ s}^{-1}$ ) similar to the determined  $k_{\text{cat}}$  ( $3.95 \text{ s}^{-1}$ ). Because with GgUox the reaction did not reach completion (figs. 4K, left panel and supplementary S8A, Supplementary Material online), reversible steps were introduced (fig. 4J). Indeed, a reaction model with three reversible steps well describes the experimental kinetics (fig. 4K, left panel). The last reaction step involves the reconversion of HIU to PIU ( $k_{-3} > k_3$ ) accounting for an equilibrium concentration of HIU never reaching the starting urate levels. Once hydrogen peroxide is formed, its concentration continues to be high in GgUox reaction compared with DrUox (figs. 4C and supplementary fig. S4, Supplementary Material online), suggesting that the last step involves the reduction of HIU without  $\text{H}_2\text{O}_2$  consumption.

### X-ray Crystallographic Analysis of Cys-rich GgUox

As GgUox displays unconventional catalytic properties, we pursued its X-ray crystallographic analysis. We crystallized GgUox in complex with its AZA inhibitor in two space groups ( $P2_12_12_1$  and  $C222_1$ ) and solved its structure at resolution values between 1.7 and 2.1 Å (see supplementary table S2, Supplementary Material online). In the crystal (fig. 5A and B), GgUox is a tetramer (dimer of dimers) as expected from SEC (see supplementary fig. S4B, Supplementary Material online) and observed in other species (Colloc'h et al. 1997; Kratzer et al. 2014; Hibi et al. 2016; Marchetti et al. 2016; Chiu et al. 2021). Electron density is generally well defined, but flexibility prevented modeling of the C-terminal region corresponding to the unique reptilian peptide extension (last 20 amino acids; see fig. 2A). The structure of GgUox is very similar to those of uricases from other organisms with typical rms deviations as assessed using the PDBeFold server (Krissinel and Henrick 2004) around 1.50 Å—the fossil euarchontoglires uricase (Kratzer et al. 2014) is the most similar one (Protein Data Bank PDB code 4MB8; r.m.s.d. 1.16 Å). Individual protomers are composed of a tandem of structurally similar tunneling-fold domains of mixed  $\alpha+\beta$  topology that form an antiparallel curved  $\beta$ -sheet with helices arranged on the convex side of the sheet. Dimerization engenders a basket-like structure that hosts two symmetric active sites contributed by residues from both chains. Recruitment of an additional dimer positioned upside-down on top of the first one and rotated by  $90^\circ$  generates the complete tetrameric assembly of D2 symmetry. Reptilian uricase displays a unique enrichment in cysteines (see figs. 2 and 3). Figure 5A and B shows that cysteine residues mostly decorate the central section of

the GgUox dimer where they are fairly homogeneously distributed.

AZA binding to GgUox is stabilized by direct hydrogen bonds with main-chain nitrogen atoms of T63\* and Y230 as well as with the side chains of R182 and Q231, and a water molecule (wN) (fig. 5C, the asterisk indicates residues belonging to a different protomer). Residues Y16\*, P62\*, D64\*, F165, L176, and S229 further line the binding pocket with the aromatic side-chain of F165 engaged in  $\pi$ -stacking with the pyrimidine ring of the inhibitor. At different stages of the uricase reaction  $\text{O}_2$  and water must occupy the “peroxo hole” above the organic substrate in proximity to the Thr-Lys catalytic dyad (T63\*-K18\* in GgUox) (Bui et al. 2014; McGregor et al. 2021). In the present structures, electron density at this location is best explained by a mixture of water molecules and  $\text{O}_2$  connected via hydrogen bonds that are generally conserved in the different GgUox active sites (fig. 5C and supplementary fig. S10, Supplementary Material online). Dioxygen interacts via H-bonds with the nearby T63\* and its stabilization is likely also promoted by the conformation of the sauropsid-specific Y230 that lines the “peroxo hole” with the hydrophobic “side” of its phenolic side chain. Of the eighteen cysteine residues of GgUox, C287, positioned directly above Q231, is in closest proximity of the “peroxo hole” whilst C14\* and C289 are further away at  $\sim 8.5$  Å from C287. All these cysteines are sauropsid-specific and conserved (see fig. 2A).

### GgUox Aggregation Upon Catalysis

In addition to those decorating the central section of the GgUox dimer, a number of cysteines are distributed on the protein surface (see fig. 5A and B). These exposed cysteines could be susceptible to  $\text{H}_2\text{O}_2$  oxidation during GgUox reaction suggesting possible interactions between tetramers. To test this hypothesis, we measured the hydrodynamic diameter of GgUox in solution during the reaction by dynamic light scattering (DLS). Measurements were done at different time points after the addition of the urate substrate. Initially, we employed reaction conditions similar to those used for the spectroscopic measurements, namely 100  $\mu\text{M}$  urate and a substrate–enzyme ratio of 5:1. Under these conditions, no aggregation was observed over a 2-h period (supplementary fig. S11A, Supplementary Material online). However, when the concentration of urate was increased to 2.1 mM, with a substrate–enzyme ratio of 100:1, the hydrodynamic diameter of GgUox increased from 12 to  $\sim 700$  nm after 5 min and stabilized at  $\sim 500$  nm within 30 min (fig. 6A, left panel). When GgUox was pre-incubated with  $\beta\text{ME}$ , no change in the hydrodynamic diameter occurred over a 1-h period (fig. 6A, right panel). By repeating the same experiments with DrUox we observed no changes in the hydrodynamic diameter either in the presence or in the absence of  $\beta\text{ME}$  (fig. 6B). These results strongly suggest that, under our experimental conditions, GgUox aggregates during the reaction most probably through the formation of disulfide bonds.



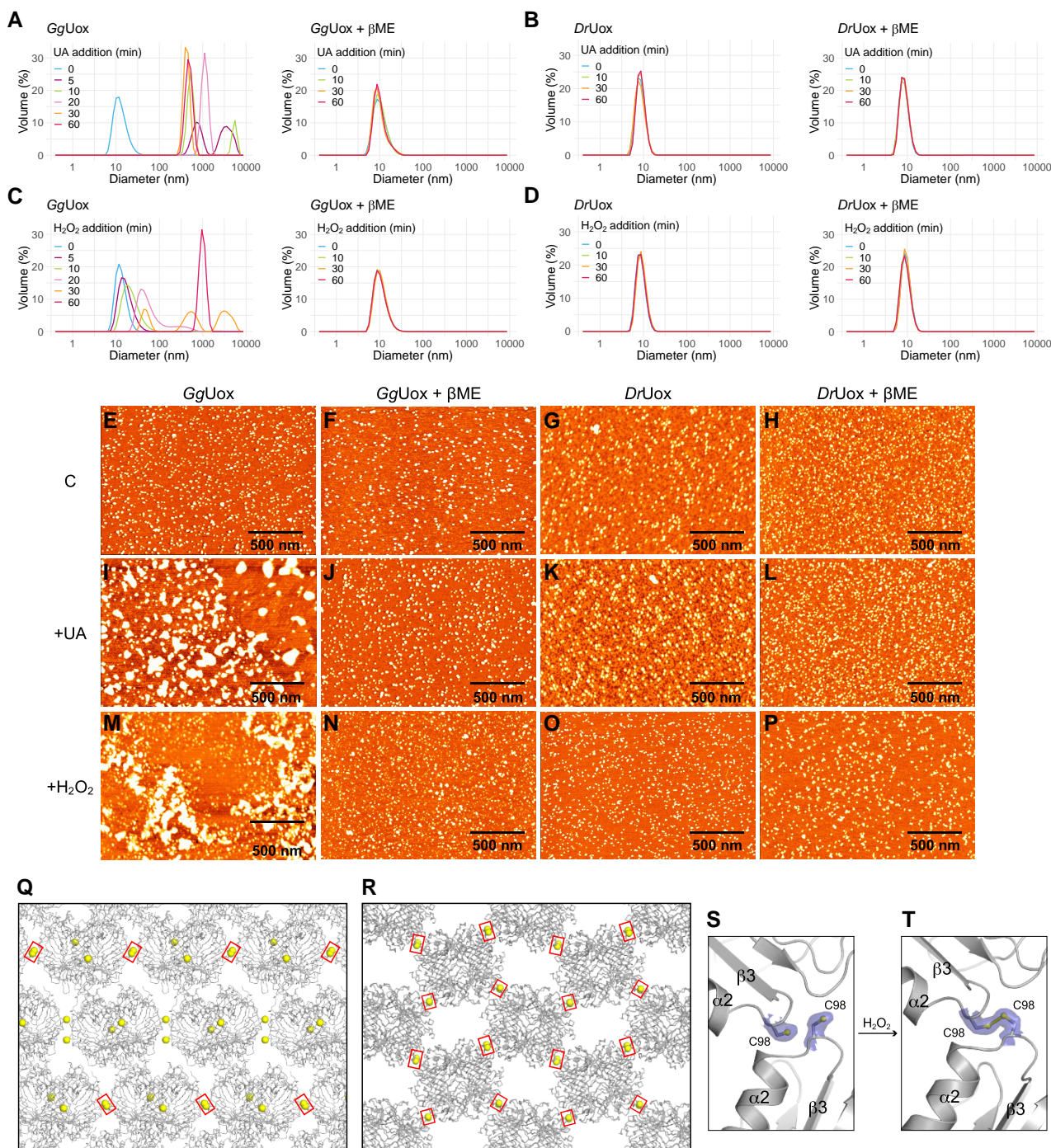


**FIG. 6.** Self-aggregation behavior of GgUox. (A and B) DLS measurements of (A) GgUox or (B) DrUox samples containing 21  $\mu\text{M}$  enzyme, and (left panel) 0 or (right panel) 300  $\mu\text{M}$   $\beta\text{ME}$  incubated at room temperature (RT) and analyzed at different time points after the addition of 2.1 mM urate (UA). The protein-substrate solutions were diluted to a protein concentration of 7  $\mu\text{M}$  before measurements. (C and D) DLS measurements of (C) GgUox or (D) DrUox samples containing 7  $\mu\text{M}$  enzyme, and (left panel) 0 or (right panel) 300  $\mu\text{M}$   $\beta\text{ME}$  incubated at RT and analyzed at different time points after the addition of 100  $\mu\text{M}$   $\text{H}_2\text{O}_2$ . (E–H) AFM 2D images of (E) GgUox not pre-incubated or (F) pre-incubated with  $\beta\text{ME}$ , and of (G) DrUox not pre-incubated or (H) pre-incubated with  $\beta\text{ME}$ . (I–L) AFM 2D images of (I and J) GgUox or (K and L) DrUox after incubation at RT with 2.1 mM UA at a substrate/enzyme ratio of 100:1, and (I and K) 0 or (J and L) 300  $\mu\text{M}$   $\beta\text{ME}$ . (M–P) AFM 2D images of (M and N) GgUox or (O and P) DrUox after incubation at RT with 100  $\mu\text{M}$   $\text{H}_2\text{O}_2$  at a substrate/enzyme ratio of 70:1, and (M and O) 0 or (N and P) 300  $\mu\text{M}$   $\beta\text{ME}$ . The protein-substrate solutions were diluted to a protein concentration of 100 nM before being deposited on the mica surface. Size bar, 500 nm. (Q and R) Packing arrangement for GgUox in space groups (Q)  $C22_1$  and (R)  $P2_12_12_1$  with surface-exposed C98 residues represented by yellow spheres. In the crystal, some, or all of them engaged in intermolecular disulfide bridges are highlighted by red rectangles. In  $C22_1$  these S–S bonds generate cross-linked linear filaments of GgUox whilst in  $P2_12_12_1$  they produce two-dimensional layers. (S and T) Representative C98-mediated intermolecular disulfide crosslinking triggered by  $\text{H}_2\text{O}_2$  treatment.  $2mF_o - DF_c$  electron density map shown in blue at the 1.0  $\sigma$  level. Going from the (S) reduced to the (T) oxidized state, the sidechain of C98 in the bottom GgUox molecule undergoes a  $\sim 120^\circ$  rotation from the *plus* to the *minus* conformer engendering a disulfide bond with a neighboring molecule.

To assess the oxidizing action of the uricase product hydrogen peroxide on Uox cysteines, we measured the particle diameter at different time points after the two enzymes were exposed to this compound. Aggregation of GgUox occurred only in the absence of  $\beta$ ME (fig. 6C), whereas aggregation of DrUox occurred neither in the absence nor in the presence of  $\beta$ ME (fig. 6D). Once formed, GgUox aggregates were unaffected by the addition of  $\beta$ ME (supplementary S11B Fig, Supplementary Material online).

In addition to DLS, atomic force microscopy (AFM) was employed for the direct visualization of Uox aggregation. First, GgUox and DrUox, under native or reducing conditions, were each deposited on a freshly cleaved mica surface (fig. 6E–H). The average particle volume measured by AFM was consistent with a tetrameric protein of ~150 kDa. No significant difference in size was observed between samples pre-incubated or not with  $\beta$ ME (supplementary fig. S12A–E, Supplementary Material online). Then, the two enzymes were each incubated for 1 h at room temperature with urate or hydrogen peroxide either in the presence or absence of  $\beta$ ME and deposited onto freshly cleaved mica (fig. 6I–P). Consistently with DLS measurements, we observed the formation of large protein aggregates only in GgUox samples incubated either with urate or hydrogen peroxide in the absence of  $\beta$ ME (fig. 6I and M and supplementary fig. S12F–G, Supplementary Material online).

The X-ray structure of GgUox suggests a possible mechanism for disulfide-mediated aggregation. GgUox was crystallized in two alternative space groups (C222<sub>1</sub> and P2<sub>1</sub>2<sub>1</sub>2<sub>1</sub>) that display a different packing arrangement (fig. 6Q and R). However, in both space groups, intermolecular contacts are, at least partly, mediated by the loop containing the saurosid-specific C98 residue, indicating that this interaction is also favored in solution. Under reducing conditions all C98 residues are seen adopting the *plus* rotamer ( $\chi_1 = 55^\circ$ ) with SG atoms from neighboring ones typically ~5.4 Å apart (fig. 6S). Upon treatment with H<sub>2</sub>O<sub>2</sub> one cysteine rotates to its *minus* rotational conformer ( $\chi_1 = -65^\circ$ ) allowing these residues to engage in disulfide bridges (fig. 6T) that in space group C222<sub>1</sub> generate linear filaments (fig. 6Q) whilst in P2<sub>1</sub>2<sub>1</sub>2<sub>1</sub> give rise to two-dimensional cross-linked arrays (fig. 6R). Exposure to H<sub>2</sub>O<sub>2</sub> also selectively oxidizes other GgUox cysteine residues. Whilst most are unmodified, residues C41, C141, C197 and C204 that are saurosid-specific (see fig. 2A) are generally seen in their sulfinic (Cys-SO<sub>2</sub>H) form, although in a few chains some of these are present as sulfenic acids (Cys-SOH), probably as intermediates to their higher oxidation state (supplementary fig. S13, Supplementary Material online).

### Uricase Gene Duplication in Chelonian Reptiles

The *Uox-Dnase2b* locus with a head-to-head arrangement is present in conserved synteny in metazoans (Mori et al. 2022). Among reptiles, chelonians (tortoises and turtles)

have a duplicate *Uox*, which we call *Uox2*, and which lies tail-to-tail with *Dnase2b* (supplementary fig. S14A, Supplementary Material online). The two paralogs are sister to each other in the *Uox* phylogeny (supplementary fig. S14B, Supplementary Material online), suggesting that the duplication event occurred within the Testudines order.

Curiously, these paralogs differ at the very active site position that distinguishes reptilian and non-reptilian *Uox*: chelonian *Uox* sequences have histidine at position 230 (relative to the GgUox sequence), whereas *Uox2* maintained the tyrosine residue (supplementary fig. S15, Supplementary Material online). In contrast, nonreptilian *Uox* has an aliphatic amino acid (in most cases valine) at that position (see fig. 2A). To evaluate the effect of these substitutions on uricase activity, we mutated the tyrosine in the active site of GgUox to either histidine (Y230H), as observed in chelonian *Uox*, or valine (Y230V), as in a canonical *Uox* sequence. For both mutants, the specific activity was decreased by ~75% compared to that of the wild-type enzyme (supplementary fig. S14C, Supplementary Material online), although no differences were observed in protein solubility (supplementary fig. S16, Supplementary Material online).

### Reptilian *Uox* is Expressed in the Skin and Shows a Punctuated Pattern in Feather Epithelium

Available RNA-sequencing (RNA-seq) data from *Gallus gallus* and another bird, *Serinus canaria*, and from the lizard *Anolis carolinensis* were analyzed to explore the expression pattern of *Uox* in adult tissues (supplementary table S3 and fig. S17, Supplementary Material online). In the two birds, we detected *Uox* expression in the skin (fig. 7A and B), particularly in the feather follicle (fig. 7A), while in the lizard, *Uox* transcripts are abundant in regenerating tail tissues (fig. 7C). *Uox* transcripts are absent in the liver at variance with nonreptiles. By contrast, high expression in the liver is maintained by *Dnase2b* and *Urah* (supplementary fig. S18, Supplementary Material online). Expression of the two *Uox* paralogs of turtles was evaluated by analyzing RNA-seq data from the species *Chelonia mydas* and *Pelodiscus sinensis* (supplementary table S4, Supplementary Material online). *Uox1* and *Uox2* transcripts are both present in the skin, with higher levels for *Uox2*, and not in the liver or kidney at variance with *Dnase2b* and *Urah* (supplementary fig. S19, Supplementary Material online).

By analyzing available data from the chicken skin transcriptome from day 6 to day 21 of embryogenesis (supplementary table S3, Supplementary Material online), we could observe the temporal variation of UOX expression and clusterize UOX co-expressed genes based on their expression profiles (supplementary fig. S20, Supplementary Material online). The resulting cluster comprises mainly feather keratins (fig. 7D). Notably, the highest expression occurs at days 13–14, consistent with the increase of gene expression observed between days 10–15 by cap analysis of gene expression (CAGE) available on Chicken-ZENBU



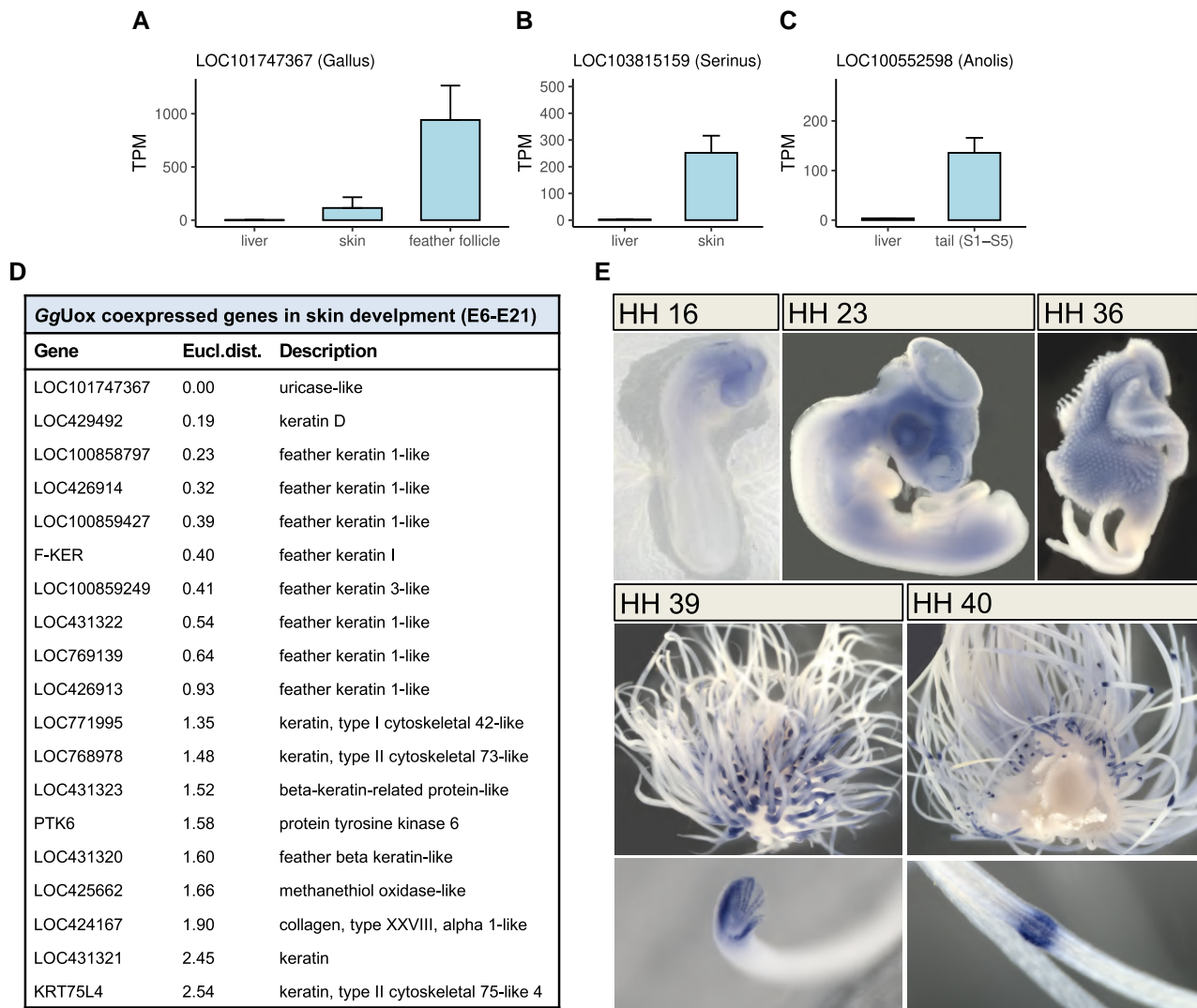


**Fig. 7.** Expression of *Uox* in reptilian skin. (A–C) *Uox* gene expression levels (TPM: Transcripts Per kilobase Million) in the liver and tegumental tissues (skin and feather follicle) of (A) *Gallus gallus*, (B) *Serinus canaria*, and (C) *Anolis carolinensis*, as derived from RNA-seq data analysis. (D) List of genes included in the same cluster as *GgUox* gene by similarity in their expression profiles in skin embryo developmental stages E6-E21. (E) In situ hybridization analysis of *UOX* expression in chick embryos at HH developmental stages 16, 23, 36, 39, and 40.

platform (Lizio et al. 2017) (supplementary fig. S21, Supplementary Material online).

To determine the pattern of *UOX* expression during embryogenesis at higher spatial resolution, whole-mount in situ hybridization analyses were performed in chicken embryos from day 2 to 15 of development corresponding to Hamburger–Hamilton (HH) stages 16–40 (Hamburger and Hamilton 1992) (fig. 7E). At HH stage 16, *UOX* expression was first detected in the head mesenchyme; at HH stage 23 it was found also in the leg and wing mesenchyme. In the next stages until HH stage 36, *UOX* mRNAs were further detected in the lung, heart, foregut, and spinal cord. At HH stages 39–40 a punctuated expression of *UOX* was detected in the feather epithelium. The punctuated expression of *UOX* during the last stages of embryo development coincides with the increase of gene expression observed by RNA-seq and CAGE analyses. During this period,

primary follicles form allowing differentiation and elongation of the feather filaments (Lucas and Stettenheim 1972). Our data are supported by recently published RNA-seq analysis showing upregulation of *UOX* expression in differentiating chicken skin epithelial cells, namely epidermal keratinocytes (Lachner et al. 2021). In parallel, the expression of *URAH* and *DNASE2B* genes was analyzed, but no staining was observed at HH stage 39 in the feather epithelium (supplementary fig. S22, Supplementary Material online).

Both RNA-seq and in situ hybridization data provide evidence that reptilian *Uox* lost expression in the liver and acquired expression in the skin, in particular in bird feather and lizard tail. *GgUox* ability to degrade urate was evaluated at slightly acidic pH values that mimic the skin environment. Although the enzyme is still active at a lower pH, no increase in the specific activity was

observed ([supplementary fig. S23, Supplementary Material online](#)).

## Discussion

Transition to uricotelism is a main vertebrate adaptation to life on land, accounting for the exquisite ability of birds and reptiles to survive in arid environments. A relevant question about the molecular basis of this physiological condition is the fate of uricase, the enzyme that in other vertebrates catalyzes the conversion of uric acid to more soluble compounds. Our study reveals a history of co-option of the uricase gene in uricotelic vertebrates that is marked by an unparalleled increase in cysteine content. Functional divergence of orthologous genes at the sequence level is known to occur through substitutions of a few amino acid residues that are crucial for the protein function ([Bartlett et al. 2003](#); [Studer et al. 2013](#)). Here, we show that a shift in the physiological role of uricase in reptiles occurred through a significant increase in the abundance of a particular amino acid (cysteine).

Through a large-scale analysis of the variation in amino acid composition among orthologs, we showed that in vertebrates the cysteine content tends to remain constant during evolution, and that Uox represents a unique case of cysteine enrichment across the two amniote lineages, sauropsids and mammals. Interestingly, the majority of cysteines were introduced in the Uox sequence after sauropsids split from stem amniotes, but before the divergence between lepidosaurs (lizards and snakes) and archelosaurs (turtles, birds, and crocodilians) ([fig. 8](#)). At this time, the evolutionary transition to uricotelism is thought to have already occurred (see [fig. 1](#)). Therefore, cysteine enrichment entailing the co-option of Uox gene is one of the molecular mechanisms that led to the establishment of uricotelism in the reptile ancestor.

Unlike cysteine, three amino acids emerged as highly variable among vertebrate orthologs: isoleucine, asparagine, and lysine. These residues are encoded by AU-rich codons and were found to be enriched in proteins from GC poor coding regions of vertebrate genomes ([Huttener et al. 2019](#)). Our findings that I, N, and K are enriched in several reptilian proteins compared to their mammalian and piscine orthologs (see [figs. 3C and D](#) and [supplementary fig. S3, Supplementary Material online](#)) are in agreement with the lower GC content measured in reptilian transcripts ([Huttener et al. 2019](#)).

Uricases are cofactor-independent oxidases ([Fetzner and Steiner 2010](#); [Bui and Steiner 2016](#)) that catalyze the two-electron oxidation of UA to HIU which is typically irreversible. In this study, we have shown that, unique amongst the uricases hitherto characterized, GgUox also reduces HIU back to UA. One appealing hypothesis for the key determinant of this unexpected feature is the rich complement of cysteine residues found in sauropsids' uricases that might provide the source of reducing equivalents required for UA regeneration. A role for thiol groups in HIU reduction has been already proposed for the

“conventional” soybean Uox ([Sarma and Tipton 2000](#)). In the presence of DTT or free cysteine, it was found that O<sub>2</sub> consumption greatly exceeded the concentration of UA in solution and that H<sub>2</sub>O<sub>2</sub> production was attenuated. This is because DTT-mediated reduction of HIU resulted in UA regeneration, with the natural substrate becoming catalytic, rather than stoichiometric, in the reaction. With GgUox, the apparent rate-enhancement of UA conversion in the presence of HIUase can be interpreted in terms of the Le Chatelier's principle with the latter enzyme able to degrade HIU once it leaves the active site. In the absence of HIUase, we propose that the many solvent-exposed cysteines act as reducing agents leading to UA regeneration thus resulting in its apparent slower rate of conversion under steady-state conditions. Our kinetic experiments with the competitive inhibitor AZA suggest, however, that HIU reduction also depends on active site residues. It is tempting to speculate that the nearby C287, as well as C14\* and C289, play a role in this process possibly via solvent-mediated electron transfer as the X-ray structure of GgUox shows that compared to the “conventional” AfUox, its “peroxo hole” ([supplementary fig. S25, Supplementary Material online](#)) is filled with a network of water molecules that might act as an electron conduit linking these cysteines with HIU. A water-mediated electron transfer involving sulfur-containing amino acids has been proposed in model peptide systems ([Wang et al. 2009](#)). Whilst an adequate understanding of the molecular mechanism underpinning the reversibility in GgUox catalysis will undoubtedly require additional studies, we propose that a key role for this is to be ascribed to the unique cysteine enrichment in reptilian uricase.

A single amino acid substitution (a tyrosine instead of an aliphatic amino acid) occurred at the reptile Uox active site. In the X-ray structure of GgUox we observed that this residue (Y230) lines the “peroxo hole” and likely stabilizes PIU contributing to the equilibrium between this intermediate and HIU. To assess the role of this mutation, we compared the activity of wild-type GgUox with that of a mutated variant having a valine at the active site position. In view of a moderate decrease in the specific activity of the mutant protein, we conclude that this substitution is not the only determinant of the reduced catalytic efficiency of GgUox.

Gene co-option may occur through changes in expression pattern instead of or in addition to functional modifications of the encoded protein ([True and Carroll 2002](#); [Rebeiz et al. 2011](#); [Malatesta et al. 2020](#)). In the case of reptilian Uox, both mechanisms are involved. The shift in gene expression from the liver to the skin was mediated by the displacement of Uox 5' exon that resulted in the loss of co-regulated transcription between Uox and the divergently oriented *Dnase2b* gene (see [fig. 2B](#)). Separation of two head-to-head genes is far from common because head-to-head gene pairs were demonstrated to largely maintain this organization enabling coordinated expression and functionality during vertebrate evolution ([Li et al. 2006](#)). The reptilian *Uox-Dnase2b* locus provides an



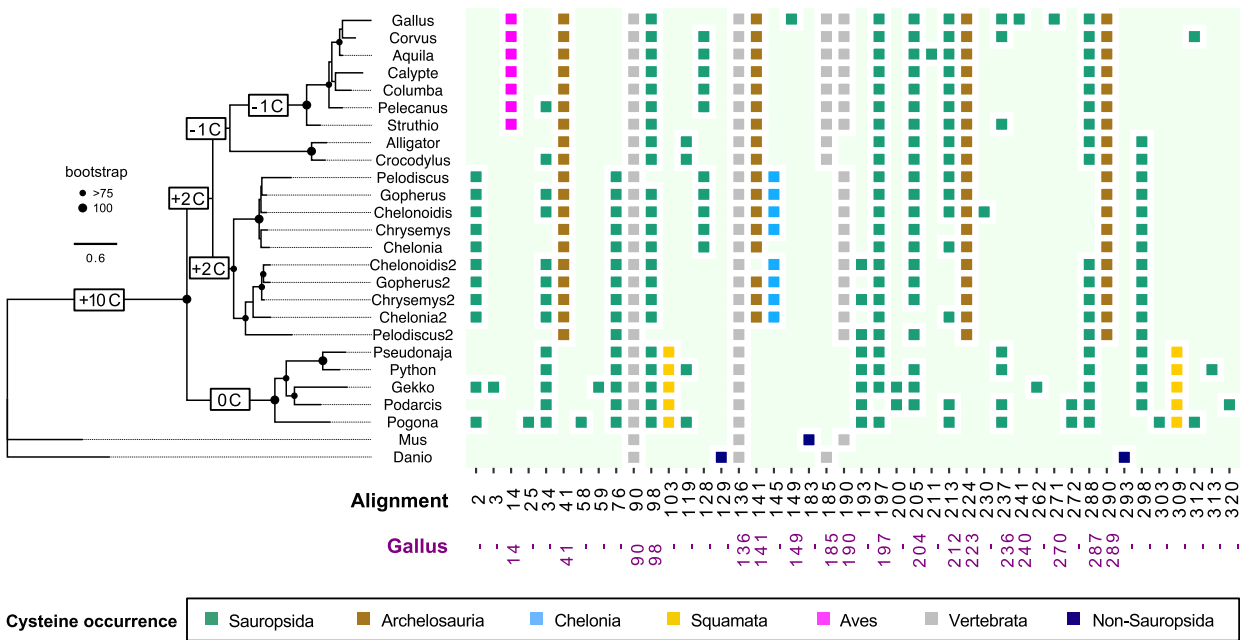


**Fig. 8.** Cysteine enrichment in the *Uox* sequence at the stem of reptile evolution. Maximum-likelihood phylogenetic tree of *Uox* sequences from vertebrate species and cysteine distribution in each sequence. *Danio rerio* *Uox* was used as an outgroup to root the tree. Bootstrap values (>75%; 100%) are indicated at internal nodes according to the legend; values below 75% are not indicated. Cysteines (C) enrichment (gain minus loss) in the *Uox* sequence during reptile evolution according to the Bayes model of ancestral sequence reconstruction (see [supplementary fig. S24, Supplementary Material](#) online) is indicated on branches. Scale bar, substitution/site. Cysteine residues are numbered according to multiple alignments (see [supplementary fig. S15, Supplementary Material](#) online) and colored according to their presence in the different lineages as indicated in the legend.

example of a mechanism by which a functional split can occur in head-to-head genes without chromosomal rearrangement. Another modification of the *Uox* locus was observed in turtles with the presence of a duplicated *Uox* copy. The presence of multiple copies of *Uox* is exceptional as this gene is typically a single copy in all genomes. Since *Uox* is a tetrameric protein, multiple gene copies could result in a heterogeneous composition of the oligomer. This hypothesis is substantiated by the co-expression of the two *Uox* paralogs in turtles' skin.

The expression of *UOX* detected in the feather epithelium of chick embryos is high at stages (around HH40; days 13–14) during which the most rapid growth of feather filaments occurs ([Meyer and Baumgärtner 1998](#)). At this time also the synthesis of keratins has started as the sheath covering the developing feather is fully keratinized after HH stage 41 ([Lucas and Stettenheim 1972](#)). Of note, apart from a protein with similarity to methanethiol oxidase (LOC425662) and two other exceptions, the list of the proteins that are co-expressed with *GgUox* in the skin of developing embryos (see [fig. 7D](#)) is entirely constituted by keratins, mostly of the  $\beta$ -type. Also in the adult, *GgUox* gene has been found in the same co-expression cluster with feather ( $\beta$ ) keratins and keratin-associated genes ([Bush et al. 2018](#)).  $\beta$ -keratins are small proteins of the stratum corneum of birds and reptiles that have a high content of cysteines (4–20%), form stacked  $\beta$ -sheets, and aggregate into very resistant microfibrils. The dense

$\beta$ -keratin matrix forms hard skin appendages, like scales, scutes, turtles' shell, claws, beaks, and feathers, providing waterproofing and mechanical protection to these structures ([Holthaus et al. 2018](#)). Interestingly, also the cysteine contents of these sauropsid-specific keratins was found to be increased during the evolution of archelosaurs ([Ehrllich et al. 2020](#)). At variance with the more widespread  $\alpha$ -keratins, the mechanism of aggregation of  $\beta$ -keratins is largely unknown ([Gregg and Rogers 1986; Alibardi et al. 2006](#)). Intriguingly, we observed a tendency to aggregate in *GgUox* which is dependent on the redox state and mediated by disulfide bond formation (see [fig. 6](#)).

Since the presence of *bona fide Uox* genes is in contrast with the uricotelism of birds and reptiles, an official gene symbol has not been established for their *Uox* orthologs, which are annotated in the sequence database with a generic "LOC" prefix followed by a numeric Gene ID. To account for the catalytic activity of the encoded protein on uric acid, but the radically different physiological role, tissue specificity, and structural features, we propose to name the *Gallus gallus* gene "cysteine-rich urate oxidase" (CRUOX).

Defining the precise physiological role of reptilian uricase is challenging. One possibility may naturally be the oxidation of urate in the skin. Uric acid, which is one of the major antioxidants in the blood, is also elevated in bird feathers ([Bolliger and Tow 1946](#)). However, the decreased catalytic efficiency and the reversibility of the

catalyzed reaction are at odds with the hypothesis that the main function of the enzyme is still urate oxidation. Another possibility may be the production of allantoin, a molecule that is reported to have skin wound healing properties (Menezes et al. 2020; Sakthiguru and Sithique 2020). Against this hypothesis, however, are the absence of OHCU decarboxylase in sauropsids and the low expression of HIU hydrolase in the skin. The production of hydrogen peroxide should also be considered as a possible function of reptilian uricase; despite its toxicity, hydrogen peroxide has several physiological roles in vertebrates (Di Marzo et al. 2018). In the skin, hydrogen peroxide may be needed in case of infections or, possibly, in the formation of the skin stratum corneum. Notably, also catalase is transcriptionally upregulated in differentiating chicken epidermal keratinocytes (Lachner et al. 2021) and this suggests that there could be a co-regulated scavenging of excess hydrogen peroxide produced by the reaction.

Sometimes a new function evolves where a new structure develops (Harlin-Cognato et al. 2006). In the case of reptilian skin, the hard appendages of the stratum corneum providing protection to the body against a dry environment, represent a clear example of innovation. The correlation between the expression of the gene and epidermal keratinocyte differentiation, a process that continues throughout the reptile's life, suggests a role for reptilian uricase in the maturation of the skin barrier. The evolutionary enrichment of the protein sequence in cysteines suggests a disulfide-mediated activity achieved under oxidizing conditions, such as those found in the outermost layer of the epidermis where oxygen exposure is maximal.

## Materials and Methods

### Amino Acid Content Variation in Vertebrate Orthologous Genes

A procedure for the analysis of the amino acid content of orthologous proteins from vertebrate species was implemented in R ([https://github.com/lab83bio/AA\\_Comp](https://github.com/lab83bio/AA_Comp)). Orthogroups were downloaded from the OrthoDB database (v. 10) and parsed with R scripts to create a filtered dataframe with only orthogroups at the Vertebrata level, in single copy, and present in 90% of species. Then, a statistical analysis was performed to calculate *P*-value (*t*-test) and Log<sub>2</sub> fold change from pairwise comparisons between the three different classes of Mammalia, Sauropsida and Actinopterygii. Volcano plots and bar plots were created using R packages “EnhancedVolcano” and “ggplot2”, respectively.

### Bioinformatics

Protein sequences were retrieved by homology search at NCBI, aligned using Clustal Omega at the EMBL-EBI webportal (<https://www.ebi.ac.uk/Tools/msa/clustalo/>) and visualized with ESPript (<https://esript.ibcp.fr/ESPript/ESPript/>) (Robert and Gouet 2014). The search for nitrogen metabolism gene sequences in complete genomes of

vertebrate and invertebrate organisms was conducted with Hidden Markov models (Eddy 1996) for individual gene families. The figure of the gene distribution map was drawn using the R language and the taxizedb (<https://docs.ropensci.org/taxizedb/>) and ggtree (Yu 2020) libraries. Maximum-Likelihood trees were constructed with PhyML v3.0 (<http://www.atgc-montpellier.fr/phyml/>) (Guindon et al. 2010) using the automated model selection procedure (Lefort et al. 2017). Nodal support was estimated by bootstrap analysis with 100 replicates. Tree images were generated with FigTree v1.4.3 (<https://github.com/rambaut/figtree/>). Ancestral sequence reconstruction was performed using four different models implemented in Phangorn (Schliep 2011): maximum parsimony (mpr), mpr with accelerated transformation (mpr\_acctran), maximum-likelihood (ml), and highest posterior probability (bayes) based on the tree of figure 8.

### Cloning, Expression, and Purification of GgUox

For the construction of GgUox expression plasmid, the uricase-like coding sequence (XM\_015290876.2) of LOC101747367 was synthesized by Genscript (USA Inc.) into pcDNA3.1+/C-(K)DYK standard vector. The sequence was PCR-amplified with specific primers (Fw: 5'-ATATGCTAGCATGAGCCAAGTGACAATTAAGG-3' and Rev: 5'-ATATCTCGAGTTATTTCCCTGGGCAGCTAC-3') and subcloned into a pET28 expression vector at NheI/XhoI sites, in frame with the N-terminal His-tag and thrombin cleavage site. For the construction of GgUoxY230V and GgUoxY230H expression plasmids, the mutated uricase-like coding sequence was synthesized by Genscript (USA Inc.) into a pET28 expression vector. All plasmids were verified by DNA sequencing and transformed into *E. coli* BL21-Codon Plus.

GgUox (wt and mutants) was expressed in auto-induction medium (Luria Broth, supplemented with 0.05% glucose and 0.2% lactose) as follows: a 1 L culture was incubated for 10 h at 30°C until OD<sub>600</sub> reached 0.6–0.8; the culture was subsequently incubated overnight at 20°C. Cells were harvested by centrifugation (20 min, 5000 × g, 4°C), and resuspended in 40 mL lysis buffer (50 mM Tris-HCl pH 7.6, 300 mM NaCl). After lysis by sonication on ice (15 min of 1 s pulse at 35% intensity/1 s pause), the soluble fraction was recovered by centrifugation (30 min, 20,000 × g, 4°C). GgUox was purified using a 5 mL His-trap Ni-NTA column (GE Healthcare) equilibrated in 50 mM Tris-HCl pH 7.6, with 300 mM NaCl, and eluted with an imidazole gradient (10–500 mM) on Äkta Fast protein liquid chromatography (GE Healthcare). The purified protein was buffer exchanged with PD-10 columns (GE Healthcare) into 100 mM potassium phosphate buffer pH 7.6, containing 150 mM NaCl. The average yield was 60 mg of GgUox per liter of culture, with >95% purity as estimated by resolution on 12% SDS-PAGE followed by staining with Coomassie blue. The final protein concentration was estimated by

absorbance at 280 nm ( $\epsilon_{280} = 35,505 \text{ M}^{-1} \text{ cm}^{-1}$ ; <https://web.expasy.org/protparam/>). Aliquots were snap-frozen in liquid nitrogen and stored at  $-80^\circ\text{C}$ .

GgUox purification through xanthine affinity chromatography was performed following the protocol previously used for DrUox purification (Marchetti et al. 2016). GgUox soluble fraction was applied to xanthine-agarose (X3128, Sigma-Aldrich) column equilibrated with 100 mM potassium phosphate pH 7.6. After washing, the protein was eluted in the same buffer containing 0.5 mM urate. An aliquot of xanthine-agarose resin was taken before elution and loaded on SDS-PAGE to confirm the specific binding of GgUox.

### Activity Assays

Catalytic activity measurements were carried out with a Jasco V-750 spectrophotometer and a quartz cuvette of 1 cm path length. Uricase activity was assayed by monitoring the absorbance at 292 nm or at 250–340 nm in the presence of 100  $\mu\text{M}$  urate in 100 mM potassium phosphate buffer, pH 7.6, at  $25^\circ\text{C}$ . The concentration of urate (flash frozen stocks at a  $\sim 5 \text{ mM}$  concentration in aqueous solution with 0.02 N NaOH) was calculated by using the molar extinction coefficient  $\epsilon_{292} = 12,650 \text{ M}^{-1} \text{ cm}^{-1}$ . To avoid the interference of the Uox reaction product, 5-HIU, which absorbs at 292 nm, *Danio rerio* (Dr) HIU hydrolase (HIUase or UraH; 0.25  $\mu\text{M}$ ) (Zanotti et al. 2006) or *Phaeodactylum tricornutum* allantoin synthase (Alls; 1.25  $\mu\text{M}$ ) (Oh et al. 2018) was added to the reaction mixture. HIUase converts HIU to 2-oxo-4-hydroxy-4-carboxy-5-ureidoimidazole (OHCU), which has negligible absorbance at 292 nm; Alls converts HIU to allantoin, which does not absorb at 292 nm.

For the measurement of uricase activity in reducing conditions, GgUox was pre-incubated with 1 mM  $\beta\text{ME}$ . The uricase activity of DrUox (Marchetti et al. 2016) was measured in the same reaction conditions for comparison. The kinetic parameters of GgUox were measured at different concentrations (2–140  $\mu\text{M}$ ) of urate, in the presence of HIUase. Data of single wavelength (292 nm) kinetics were fitted to the Michaelis–Menten equation using the R package “drc”.

The reverse reaction of HIU to urate was performed as follows: HIU was synthesized enzymatically from urate (500  $\mu\text{M}$ ) in the presence of an excess of DrUox (20  $\mu\text{M}$ ); the reaction was carried out in 100 mM potassium phosphate buffer, pH 7.6, at room temperature for 5 min, and monitored by UV spectra (250–350 nm). When the synthesis was completed, as determined by the shift of the urate peak from 292 to 301 nm, the reaction mixture was filtered through a centrifugal membrane filter (cutoff 10,000 Da MW) to remove DrUox. GgUox (30  $\mu\text{M}$ ) pre-incubated with  $\beta\text{ME}$  (300  $\mu\text{M}$ ) was added to HIU (60  $\mu\text{M}$ ) to start the reverse reaction. UV spectra were recorded from 250 to 350 nm. Spontaneous, nonenzymatic degradation of HIU was measured by adding either 100 mM potassium phosphate buffer or DrUox (30  $\mu\text{M}$ ) pre-incubated with  $\beta\text{ME}$  (300  $\mu\text{M}$ ) to the filtered reaction

mixture. Both the urate oxidation to HIU and the reverse reaction were assayed in the presence of the urate oxidase inhibitor 8-AZA (11460, Sigma-Aldrich), which was added to the reaction mixture at a final concentration of 50  $\mu\text{M}$ .

### Stopped Flow Kinetics

Stopped flow experiments were carried out using an Applied Photophysics SX18 apparatus, with an instrumental dead time of 1.5 ms, equipped with a thermostatted bath set at  $25^\circ\text{C}$ . GgUox or DrUox solutions at 70  $\mu\text{M}$  concentration in 100 mM potassium phosphate buffer, pH 7.6, were mixed 1:1 with 50  $\mu\text{M}$  urate in a single turnover condition, and spectral changes were followed in the UV-visible range through a photodiode array. The time interval between spectra acquisitions was logarithmically distributed to have a higher acquisition rate (one spectrum every 1 ms) in the early phase, avoiding oversampling at longer time. To improve signal-to-noise ratio at least three kinetic traces were averaged.

Three-step (irreversible and reversible) models generation and data fitting to the models were carried out by exploiting the Simbiology tool (MATLAB). All other data processing was carried out using MATLAB R2020b.

### Hydrogen Peroxide Quantification

Hydrogen peroxide produced in the urate oxidation reaction catalyzed by GgUox or DrUox was quantified by Ferrous Oxidation Xylenol Orange (FOX) assay (Wolff 1994). GgUox (30  $\mu\text{M}$ ) or DrUox (30  $\mu\text{M}$ ) was incubated with urate (25  $\mu\text{M}$ ) in 100 mM potassium phosphate buffer, pH 7.6, in the absence or presence of HIUase (0.25  $\mu\text{M}$ ). At time intervals (0, 2, 5, 10, 15, 30, and 60 min after urate oxidase addition) 20  $\mu\text{L}$ -aliquots were taken and added to 200  $\mu\text{L}$  FOX1 reagent (100  $\mu\text{M}$  xylenol orange, 250  $\mu\text{M}$  ammonium ferrous sulfate, 100 mM sorbitol, 25 mM  $\text{H}_2\text{SO}_4$ ) in a 96-well plate and incubated for a minimum of 40 min at RT. The absorbance was read at 595 nm using an iMark microplate absorbance reader (Bio-rad). Each condition was conducted in triplicate. Concentrations of hydrogen peroxide were calculated from the absorbance at 595 nm using a regression equation and a correlation coefficient obtained experimentally from a standard curve. The standard curve (absorbance at 595 nm versus hydrogen peroxide concentration) was developed under the same conditions except that enzyme was not added and that dilutions of a hydrogen peroxide solution (8.8 M) were used as standards (final concentrations in the 200  $\mu\text{L}$  assay: 10, 25, 50, 100  $\mu\text{M}$ ).

### X-Ray Crystallography

Although the cloning strategy employed allows for thrombin-mediated cleavage of the engineered N-terminal His affinity tag, all crystallographic work was carried out with an uncleaved version of the protein. Protein purification was performed using a combination of Ni-affinity and Superdex 75 size-exclusion chromatographic (SEC) steps. GgUox eluted from SEC in 50 mM Tris-HCl pH 8.0,



10 mM NaCl, 1 mM tris(2-carboxyethyl)phosphine-HCl buffer was concentrated to 22 mg/mL and mixed with a 20-fold molar excess of the AZA inhibitor. Sitting-drop vapor diffusion crystallization experiments were set up at 18°C using a 1:1 protein:reservoir ratio dispensed with the Mosquito liquid handler (TTP Labtech). Single crystals of the GgUox-AZA complex were obtained after 2–3 days in the alternative orthorhombic space groups  $C22_1$  or  $P2_12_12_1$  using 8% PGA-LM, 0.3 M KBr, 0.1 M Tris-HCl pH 7.8 or 0.8 M K/Na tartrate tetrahydrate, 0.1 M HEPES pH 7.5 as crystallization reservoirs, respectively. For cryoprotection, crystals were transferred to their reservoir solution enriched with 20% ethylene glycol for a few minutes and then rapidly quenched and stored in liquid nitrogen. To probe oxidative conditions, crystals were transferred into cryoprotective solutions supplemented with 100 mM  $H_2O_2$  for 15 min before cryocooling in liquid nitrogen. Complete datasets for reduced and oxidized GgUox-AZA complexes in both available space groups were measured at beamlines I24 and I04 of Diamond Light Source (Didcot, UK). Structure solution starting from the *Aspergillus flavus* Uox model (PDB code 7A0L) (McGregor et al. 2021) was accomplished using the molecular replacement method with the Phaser package (McCoy et al. 2007) as implemented in the CCP4 suite (Winn et al. 2011). The programs COOT (Emsley and Cowtan 2004) and Refmac5 (Steiner et al. 2003; Vagin et al. 2004; Murshudov et al. 2011) were used throughout for model rebuilding and refinement, respectively. Data collection and refinement statistics are available in [supplementary table S2, Supplementary Material](#) online. Atomic coordinates and structure factors have been deposited in the Protein Data Bank with entry codes 8OFK, 8OH8, 8OIH, and 8OIW.

### Dynamic Light Scattering

DLS experiments were carried out with a Malvern Zetasizer NANO ZSP (Malvern Panalytical, Malvern, UK), at 25°C, using a plastic cuvette. To measure the hydrodynamic diameter distribution of Uox treated with  $H_2O_2$ , a solution containing 7  $\mu$ M GgUox or DrUox, pre-treated with 0 or 100  $\mu$ M  $\beta$ ME, was incubated with 100  $\mu$ M  $H_2O_2$  in 100 mM potassium phosphate buffer at pH 7.6. DLS spectra were recorded at different time points from 0 to 60 min. To measure the hydrodynamic diameter distribution of Uox during urate oxidation, a solution containing 21  $\mu$ M GgUox or DrUox, pretreated with 0 or 300  $\mu$ M  $\beta$ ME, was incubated with 2.1 mM urate in 100 mM potassium phosphate buffer at pH 7.6. DLS spectra were recorded at different time points (0–60 min) after diluting the reaction to a final protein concentration of 7  $\mu$ M. The data were analyzed with the Malvern Zetasizer software v8.1 using standard settings.

### Atomic Force Microscopy

Atomic force microscopy (AFM) images ( $512 \times 512$  pixels with a scan size of 2  $\mu$ m) were collected in air with a

Nanoscope IIIA microscope (Digital Instruments, Santa Barbara, CA, USA) operating in tapping mode and equipped with the E scanner. Commercial silicon cantilevers (MikroMasch, Tallinn, Estonia) with a nominal tip radius of 5 nm were used. In the first set of experiments, 21  $\mu$ M GgUox or DrUox pre-incubated with 0 or 300  $\mu$ M  $\beta$ ME was mixed with 2.1 mM urate in 100 mM potassium phosphate buffer, pH 7.6, and incubated at RT for 60 min. In a second set, 7  $\mu$ M GgUox or DrUox pre-incubated with 0 or 100  $\mu$ M  $\beta$ ME was mixed with 100  $\mu$ M  $H_2O_2$  in 100 mM potassium phosphate buffer, pH 7.6, and incubated at RT for 60 min. All samples were diluted in deposition buffer (4 mM HEPES pH 7.4, 10 mM NaCl, 2 mM  $MgCl_2$ ) to a final protein concentration of 100 nM, and 20  $\mu$ l were deposited onto freshly cleaved mica that had been previously incubated with 50  $\mu$ l MilliQ water for 5 min, and with 50  $\mu$ l deposition buffer for 3 min. After 5 min incubation, the excess sample on the mica surface was removed by rinsing with 50  $\mu$ l MilliQ water and drying under a nitrogen flux.

### RNA-Seq Analysis

Paired-end RNA-seq reads of liver or skin samples from different reptiles were retrieved by keyword searches and downloaded from the European Nucleotide Archive (ENA) database ([supplementary tables S3 and S4, Supplementary Material](#) online). Gene expression was quantified as transcripts per million (TPM) with Kallisto (v.0.44.0) (Bray et al. 2016) using indexes built on the transcriptomes of *Gallus gallus* (GCF\_016699485.2), *Anolis carolinensis* (GCF\_000090745.1), *Serinus canaria* (GCF\_022539315.1), *Pelodiscus sinensis* (GCF\_000230535.1), and *Chelonia mydas* (GCF\_015237465.2). Principal component analysis was conducted with the variance stabilizing transformation (vst) and PCAplot functions or the DESeq2 R package (Love et al. 2014). Plots for expression levels of individual genes were obtained with IsoformSwitchAnalyzeR (Vitting-Seerup and Sandelin 2019). Cluster analysis of gene expression profiles was conducted with the hclust and cutree ( $k = 100$ ) functions of the R package.

### Embryo Collection and In Situ Hybridization

Fertile chicken eggs (HyLine, low; not a commercially available source) were incubated in a humidified incubator at 37.5°C for 0.5–5 days. Embryos were collected into chilled chick saline (123 mM NaCl), removed from the vitelline membrane, and cleaned of yolk. Extra-embryonic membranes and large body cavities (brain vesicles, atria, allantois, eye) were opened to minimize trapping of the in situ reagents. Embryos were fixed overnight at 4°C in freshly prepared 4% paraformaldehyde in PBS, washed twice briefly in PBS plus 0.1% Triton X-100 then dehydrated through a graded methanol (MeOH) series and stored at –20°C overnight in 100% MeOH. cDNA templates for generating all antisense RNA probes were obtained by reverse transcriptase-polymerase chain reaction using pooled RNA from embryos between HH stages 4 and 40. Primer



sequences were designed using the mRNA sequence in the NCBI database. The sequence 5'-AATTAACCCTCACTAAAGG-3', corresponding to the T3 DNA polymerase binding site, was added to the 5' end of each reverse primer. The following primers were used: LOC101747367 (1089t): Forward, 5'-ATAAACCTCTGGCTTCCTG-3', Reverse, 5'-AATTAACCCTCACTAAAGGATATGGTGCAGGACGTTATC-3'. Embryo processing, antisense RNA probe preparation, and whole-mount In Situ Hybridizations were performed as described (Antin et al. 2010). A detailed protocol is available for download at <http://geisha.arizona.edu>.

## Supplementary Material

Supplementary data are available at *Molecular Biology and Evolution* online.

## Acknowledgments

We thank Davide Cavazzini and Marialaura Marchetti for assistance, Francesco Trigianta and Luciano Macaluso for their help in the initial phase of the work, and Lorenzo Alibardi for valuable discussions. Scientists and staff at Diamond Light Source (Didcot, UK) are gratefully acknowledged for their support. This work benefited from the equipment and framework of the COMP-HUB and COMP-R initiatives, funded by the “Departments of Excellence” program of the Italian Ministry for University and Research (MIUR, 2018-2022 and MUR, 2023-2027), and from the High Performance Computing facility of the University of Parma, Italy. G.M. is a recipient of post-doctoral fellowships from COMP-HUB. This work was supported by the Italian Ministry for Education, University and Research PRIN grant 2017483NH8 to R.P. and by the United Kingdom Biotechnology and Biological Sciences Research Council (BBSRC) grant BB/P000169/1 awarded to R.A.S.

## Data Availability

The datasets and computer code used in this study are available in GitHub at the address: [https://github.com/lab83bio/AA\\_Comp](https://github.com/lab83bio/AA_Comp).

## References

- Alibardi L, Dalla Valle L, Toffolo V, Toni M. 2006. Scale keratin in lizard epidermis reveals amino acid regions homologous with avian and mammalian epidermal proteins. *Anat Rec A Discov Mol Cell Evol Biol*. **288A**:734–752.
- Ames BN, Cathcart R, Schwiers E, Hochstein P. 1981. Uric acid provides an antioxidant defense in humans against oxidant- and radical-caused aging and cancer: a hypothesis. *Proc Natl Acad Sci*. **78**:6858–6862.
- Antin PB, Pier M, Sesepasara T, Yatskievych TA, Darnell DK. 2010. Embryonic expression of the chicken Krüppel-like (KLF) transcription factor gene family. *Dev Dyn*. **239**:1879–1887.
- Bartlett GJ, Borkakoti N, Thornton JM. 2003. Catalysing new reactions during evolution: economy of residues and mechanism. *J Mol Biol*. **331**:829–860.
- Bolliger A, Tow AJ. 1946. Uric acid in birds' feathers. *Aust J Sci*. **8**:131.
- Bray NL, Pimentel H, Melsted P, Pachter L. 2016. Near-optimal probabilistic RNA-seq quantification. *Nat Biotechnol*. **34**:525–527.
- Bui S, Steiner RA. 2016. New insight into cofactor-free oxygenation from combined experimental and computational approaches. *Curr Opin Struct Biol*. **41**:109–118.
- Bui S, von Stetten D, Jambrina PG, Prangé T, Colloc'h N, de Sanctis D, Royant A, Rosta E, Steiner RA. 2014. Direct evidence for a peroxide intermediate and a reactive enzyme-substrate-dioxygen configuration in a cofactor-free oxidase. *Angew Chem Int Ed*. **53**:13710–13714.
- Bush SJ, Freem L, MacCallum AJ, O'Dell J, Wu C, Afrasiabi C, Psifidi A, Stevens MP, Smith J, Summers KM, et al. 2018. Combination of novel and public RNA-seq datasets to generate an mRNA expression atlas for the domestic chicken. *BMC Genomics*. **19**:594.
- Campbell JW, Vorhaben JE, Smith DD. 1987. Uricotely: its nature and origin during the evolution of tetrapod vertebrates. *J Exp Zool*. **243**:349–363.
- Chiu Y-C, Hsu T-S, Huang C-Y, Hsu C-H. 2021. Structural and biochemical insights into a hyperthermostable urate oxidase from *Thermobispora bispora* for hyperuricemia and gout therapy. *Int J Biol Macromol*. **188**:914–923.
- Colloc'h N, El Hajji M, Bachet B, L'Hermite G, Schiltz M, Prangé T, Castro B, Morron J-P. 1997. Crystal structure of the protein drug urate oxidase-inhibitor complex at 2.05 Å resolution. *Nat Struct Biol*. **4**:947–952.
- Dembech E, Malatesta M, De Rito C, Mori G, Cavazzini D, Secchi A, Morandin F, Percudani R. 2023. Identification of hidden associations among eukaryotic genes through statistical analysis of co-evolutionary transitions. *Proc Natl Acad Sci*. **120**:e2218329120.
- Dessauer HC. 1970. Blood chemistry of reptiles: physiological and evolutionary aspects. In: *The biology of the reptilia*. Vol. 3. New York (NY): Academic Press. p. 1–72.
- Di Marzo N, Chisci E, Giovannoni R. 2018. The role of hydrogen peroxide in redox-dependent signaling: homeostatic and pathological responses in mammalian cells. *Cells*. **7**:156.
- Eddy SR. 1996. Hidden markov models. *Curr Opin Struct Biol*. **6**:361–365.
- Ehrlich F, Lachner J, Hermann M, Tschachler E, Eckhart L. 2020. Convergent evolution of cysteine-rich keratins in hard skin appendages of terrestrial vertebrates. *Mol Biol Evol*. **37**:982–993.
- Emsley P, Cowtan K. 2004. Coot: model-building tools for molecular graphics. *Acta Crystallogr D Biol Crystallogr*. **60**:2126–2132.
- Fetzner S, Steiner RA. 2010. Cofactor-independent oxidases and oxygenases. *Appl Microbiol Biotechnol*. **86**:791–804.
- Gregg K, Rogers GE. 1986. Feather keratin: composition, structure and biogenesis. In: Bereiter-Hahn J, Matoltsy AG and Richards KS, editors. *Biology of the integument: 2 vertebrates*. Berlin, Heidelberg: Springer. p. 666–694.
- Guindon S, Dufayard J-F, Lefort V, Anisimova M, Hordijk W, Gascuel O. 2010. New algorithms and methods to estimate maximum-likelihood phylogenies: assessing the performance of PhyML 3.0. *Syst Biol*. **59**:307–321.
- Hamburger V, Hamilton HL. 1992. A series of normal stages in the development of the chick embryo. *Dev Dyn*. **195**:231–272.
- Harlin-Cognato A, Hoffman EA, Jones AG. 2006. Gene cooption without duplication during the evolution of a male-pregnancy gene in pipefish. *Proc Natl Acad Sci USA*. **103**(51):19407–19412. <http://dx.doi.org/10.1073/pnas.0603000103>
- Hayashi S, Fujiwara S, Noguchi T. 2000. Evolution of urate-degrading enzymes in animal peroxisomes. *Cell Biochem Biophys*. **32 Spring**:123–129.
- Heitaroh I, Itaru Y, Eiichi G, Kyoji M, Mitsutaka N, Keiko S. 1973. Potent competitive uricase inhibitors—2,8-diazahypoxanthine and related compounds. *Biochem Pharmacol*. **22**:2237–2245.
- Hibi T, Kume A, Kawamura A, Itoh T, Fukada H, Nishiya Y. 2016. Hyperstabilization of tetrameric Bacillus sp. TB-90 urate oxidase by introducing disulfide bonds through structural plasticity. *Biochemistry*. **55**:724–732.

- Holthaus KB, Eckhart L, Dalla Valle L, Alibardi L. 2018. Review: evolution and diversification of corneous beta-proteins, the characteristic epidermal proteins of reptiles and birds. *J Exp Zool B Mol Dev Evol.* **330**:438–453.
- Huttner R, Thorrez L, in't Veld T, Granvik M, Snoeck L, Van Lommel L, Schuit F. 2019. GC Content of vertebrate exome landscapes reveal areas of accelerated protein evolution. *BMC Evol Biol.* **19**:144.
- Kahn K, Tipton PA. 1998. Spectroscopic characterization of intermediates in the urate oxidase reaction. *Biochemistry.* **37**:11651–11659.
- Keebaugh AC, Thomas JW. 2010. The evolutionary fate of the genes encoding the purine catabolic enzymes in hominoids, birds, and reptiles. *Mol Biol Evol.* **27**:1359–1369.
- Kratzer JT, Lanaspá MA, Murphy MN, Cicerchi C, Graves CL, Tipton PA, Ortlund EA, Johnson RJ, Gaucher EA. 2014. Evolutionary history and metabolic insights of ancient mammalian uricases. *Proc Natl Acad Sci.* **111**:3763–3768.
- Krissinel E, Henrick K. 2004. Secondary-structure matching (SSM), a new tool for fast protein structure alignment in three dimensions. *Acta Crystallogr D Biol Crystallogr.* **60**:2256–2268.
- Lachner J, Derdak S, Mlitz V, Wagner T, Holthaus KB, Ehrlich F, Mildner M, Tschachler E, Eckhart L. 2021. An in vitro model of avian skin reveals evolutionarily conserved transcriptional regulation of epidermal barrier formation. *J Invest Dermatol.* **141**:2829–2837.
- Lefort V, Longueville J-E, Gascuel O. 2017. SMS: smart model selection in PhyML. *Mol Biol Evol.* **34**:2422–2424.
- Li Z, Hoshino Y, Tran L, Gaucher EA. 2022. Phylogenetic articulation of uric acid evolution in mammals and how it informs a therapeutic uricase. *Mol Biol Evol.* **39**:msab312.
- Li Y-Y, Yu H, Guo Z-M, Guo T-Q, Tu K, Li Y-X. 2006. Systematic analysis of head-to-head gene organization: evolutionary conservation and potential biological relevance. *PLoS Comput Biol.* **2**:e74.
- Lizio M, Deviatiiarov R, Nagai H, Galan L, Arner E, Itoh M, Lassmann T, Kasukawa T, Hasegawa A, Ros MA, et al. 2017. Systematic analysis of transcription start sites in avian development. *PLoS Biol.* **15**:e2002887.
- Love MI, Huber W, Anders S. 2014. Moderated estimation of fold change and dispersion for RNA-Seq data with DESeq2. *Genome Biol.* **15**:550.
- Lucas AM, Stettenheim PR. 1972. Avian Anatomy Integument. Avian Anatomy Project, Poultry Research Branch, Animal Science Research Division, Agricultural Research Service, U.S. Department of Agriculture.
- Malatesta M, Mori G, Acquotti D, Campanini B, Peracchi A, Antin PB, Percudani R. 2020. Birth of a pathway for sulfur metabolism in early amniote evolution. *Nat Ecol Evol.* **4**:1239–1246.
- Marchetti M, Liuzzi A, Fermi B, Corsini R, Folli C, Speranzini V, Gandolfi F, Bettati S, Ronda L, Cendron L, et al. 2016. Catalysis and structure of zebrafish urate oxidase provide insights into the origin of hyperuricemia in hominoids. *Sci Rep.* **6**:38302.
- McCoy AJ, Grosse-Kunstleve RW, Adams PD, Winn MD, Storoni LC, Read RJ. 2007. Phaser crystallographic software. *J Appl Crystallogr.* **40**:658–674.
- McGregor L, Foldes T, Bui S, Moulin M, Coquelle N, Blakeley MP, Rosta E, Steiner RA. 2021. Joint neutron/X-ray crystal structure of a mechanistically relevant complex of perdeuterated urate oxidase and simulations provide insight into the hydration step of catalysis. *IUCrJ.* **8**:46–59.
- McLennan DA. 2008. The concept of co-option: why evolution often looks miraculous. *Evol Educ Outreach.* **1**:247–258.
- Menezes JESA, Santos Hd, Ferreira MKA, Magalhães FEA, da Silva DS, Bandeira PN, Saraiva GD, Pessoa ODL, Ricardo NMPS, Cruz BG, et al. 2020. Preparation, structural and spectroscopic characterization of chitosan membranes containing allantoin. *J Mol Struct.* **1199**:126968.
- Meyer W, Baumgärtner G. 1998. Embryonal feather growth in the chicken. *J Anat.* **193**:611–616.
- Mori G, Delfino D, Pibiri P, Rivetti C, Percudani R. 2022. Origin and significance of the human DNase repertoire. *Sci Rep.* **12**:10364.
- Murshudov GN, Skubák P, Lebedev AA, Pannu NS, Steiner RA, Nicholls RA, Winn MD, Long F, Vagin AA. 2011. REFMAC5 For the refinement of macromolecular crystal structures. *Acta Crystallogr D Biol Crystallogr.* **67**:355–367.
- Nishikimi M, Fukuyama R, Minoshima S, Shimizu N, Yagi K. 1994. Cloning and chromosomal mapping of the human nonfunctional gene for L-gulonono-gamma-lactone oxidase, the enzyme for L-ascorbic acid biosynthesis missing in man. *J Biol Chem.* **269**:13685–13688.
- Nishimura H, Yoshida K, Yokota Y, Matsushima A, Inada Y. 1982. Physicochemical properties and states of sulfhydryl groups of uricase from *Candida utilis*. *J Biochem (Tokyo).* **91**:41–48.
- Noguchi T, Takada Y, Fujiwara S. 1979. Degradation of uric acid to urea and glyoxylate in peroxisomes. *J Biol Chem.* **254**:5272–5275.
- Oda M, Satta Y, Takenaka O, Takahata N. 2002. Loss of urate oxidase activity in hominoids and its evolutionary implications. *Mol Biol Evol.* **19**:640–653.
- Oh J, Liuzzi A, Ronda L, Marchetti M, Corsini R, Folli C, Bettati S, Rhee S, Percudani R. 2018. Diatom allantoin synthase provides structural insights into natural fusion protein therapeutics. *ACS Chem Biol.* **13**:2237–2246.
- Peterson DW, Hamilton WH, Lilyblade AL. 1971. Hereditary susceptibility to dietary induction of gout in selected lines of chickens. *J Nutr.* **101**:347–354.
- Ramazzina I, Folli C, Secchi A, Berni R, Percudani R. 2006. Completing the uric acid degradation pathway through phylogenetic comparison of whole genomes. *Nat Chem Biol.* **2**:144–148.
- Rebeiz M, Jikomes N, Kassner VA, Carroll SB. 2011. Evolutionary origin of a novel gene expression pattern through co-option of the latent activities of existing regulatory sequences. *Proc Natl Acad Sci.* **108**:10036–10043.
- Robert X, Gouet P. 2014. Deciphering key features in protein structures with the new ENDscript server. *Nucleic Acids Res.* **42**:W320–W324.
- Rothschild BM, Schultze H-P, Pellegrini R, Brinkman DB, Holroyd PA, Gardner JD. 2013. Osseous and other hard tissue pathologies in turtles and abnormalities of mineral deposition. In: *Morphology and evolution of turtles. Vertebrate paleobiology and paleoanthropology*. Dordrecht: Springer Netherlands. p. 501–534.
- Rothschild BM, Tanke D, Carpenter K. 1997. Tyrannosaurs suffered from gout. *Nature.* **387**:357–357.
- Sakthiguru N, Sithique MA. 2020. Fabrication of bioinspired chitosan/gelatin/allantoin biocomposite film for wound dressing application. *Int J Biol Macromol.* **152**:873–883.
- Salway JG. 2018. The Krebs uric acid cycle: a forgotten Krebs cycle. *Trends Biochem Sci.* **43**:847–849.
- Sarma AD, Tipton PA. 2000. Evidence for urate hydroperoxide as an intermediate in the urate oxidase reaction. *J Am Chem Soc.* **122**:11252–11253.
- Schliep KP. 2011. Phangorn: phylogenetic analysis in R. *Bioinformatics.* **27**:592–593.
- Sharma V, Hiller M. 2020. Losses of human disease-associated genes in placental mammals. *NAR Genomics Bioinforma.* **2**:lqz012.
- Simic MG, Jovanovic SV. 1989. Antioxidation mechanisms of uric acid. *J Am Chem Soc.* **111**:5778–5782.
- Singer MA. 2003. Do mammals, birds, reptiles and fish have similar nitrogen conserving systems? *Comp Biochem Physiol B Biochem Mol Biol.* **134**:543–558.
- Steiner RA, Lebedev AA, Murshudov GN. 2003. Fisher's information in maximum-likelihood macromolecular crystallographic refinement. *Acta Crystallogr D Biol Crystallogr.* **59**:2114–2124.
- Studer RA, Dessailly BH, Orengo CA. 2013. Residue mutations and their impact on protein structure and function: detecting beneficial and pathogenic changes. *Biochem J.* **449**:581–594.
- True JR, Carroll SB. 2002. Gene co-option in physiological and morphological evolution. *Annu Rev Cell Dev Biol.* **18**:53–80.
- Vagin AA, Steiner RA, Lebedev AA, Potterton L, McNicholas S, Long F, Murshudov GN. 2004. REFMAC5 Dictionary: organization of

- prior chemical knowledge and guidelines for its use. *Acta Crystallogr D Biol Crystallogr.* **60**:2184–2195.
- Vitting-Seerup K, Sandelin A. 2019. Isoformswitchanalyzer: analysis of changes in genome-wide patterns of alternative splicing and its functional consequences. *Bioinformatics.* **35**:4469–4471.
- Wang M, Gao J, Müller P, Giese B. 2009. Electron transfer in peptides with cysteine and methionine as relay amino acids. *Angew Chem Int Ed.* **48**:4232–4234.
- Winn MD, Ballard CC, Cowtan KD, Dodson EJ, Emsley P, Evans PR, Keegan RM, Krissinel EB, Leslie AGW, McCoy A, et al. 2011. Overview of the CCP4 suite and current developments. *Acta Crystallogr D Biol Crystallogr.* **67**:235–242.
- Wolff SP. 1994. [18] Ferrous ion oxidation in presence of ferric ion indicator xylenol orange for measurement of hydroperoxides. *Meth Enzymol.* **233**:182–189.
- Wright PA. 1995. Nitrogen excretion: three end products, many physiological roles. *J Exp Biol.* **198**:273–281.
- Wu XW, Lee CC, Muzny DM, Caskey CT. 1989. Urate oxidase: primary structure and evolutionary implications. *Proc Natl Acad Sci.* **86**:9412–9416.
- Yu G. 2020. Using ggtree to visualize data on tree-like structures. *Curr Protoc Bioinforma.* **69**:e96.
- Zanotti G, Cendron L, Ramazzina I, Folli C, Percudani R, Berni R. 2006. Structure of zebra fish HIUase: insights into evolution of an enzyme to a hormone transporter. *J Mol Biol.* **363**:1–9.